Gernot Gruber, BSc

Characterization of point defects in semiconductors using electrically detected magnetic resonance

MASTER THESIS

For obtaining the academic degree
Diplom-Ingenieur

Master Programme of
Technical Physics

Graz University of Technology

Supervisor:

Univ.-Prof. Ph.D. Peter Hadley

Institute of Solid State Physics

Co-Supervisor:

Ass.Prof. Dipl.-Ing. Dr.techn. Markus Koch

Institute of Experimental Physics

Graz, August 2012

Deutsche Fassung:
Beschluss der Curricula-Kommission für Bachelor-, Master- und Diplomstudien vom 10.11.2008
Genehmigung des Senates am 1.12.2008

EIDESSTATTLICHE ERKLÄRUNG

Ich erkläre an Eides statt, dass ich die vorliegende Arbeit selbstständig verfasst, andere als die angegebenen Quellen/Hilfsmittel nicht benutzt, und die den benutzten Quellen wörtlich und inhaltlich entnommene Stellen als solche kenntlich gemacht habe.

Graz, am ……. ……..
(Unterschrift)

Englische Fassung:

STATUTORY DECLARATION

I declare that I have authored this thesis independently, that I have not used other than the declared sources / resources, and that I have explicitly marked all material which has been quoted either literally or by content from the used sources.

……. ……..
date (signature)

Kurzfassung

Defekte spielen eine wichtige Rolle für die Verlässlichkeit und Haltbarkeit von Halbleitern. Die Charakterisierung und Identifizierung von Defekten ist schwierig und von immer größerem Interesse für die Halbleiterindustrie. Diese Arbeit beschäftigt sich mit der Untersuchung von Punktdefekten durch die Methode der elektrisch detektierten Magnetresonanz (EDMR).

Das Auftreten von Defekten ist unvermeindbar. Jedoch eröffnet Wissen über ihre Gestalt die Möglichkeit Prozesse hinsichtlich der Minimierung ihrer Konzentration zu adaptieren. Eine der wenigen Methoden zur Charakterisierung von Punktdefekten ist EDMR. Diese Methode kombiniert Elektronspinresonanz (ESR) mit elektrischen Messungen und erlaubt die strukturelle Untersuchung von Defekten in voll prozessierten Halbleiterbauteilen. Der Vorteil liegt einerseits in der Messbarkeit geringerer Konzentrationen und andererseits in der Möglichkeit der selektiven Untersuchung bestimmter Bereiche eines Bauteils. Dies können beispielsweise die Verarmungsregion eines pn-Übergangs oder die Grenzschicht zwischen Silizium und Gateoxid eines MOSFETs sein.

Ziel dieser Arbeit war es einen bestehenden ESR Aufbau hinsichtlich der Möglichkeit von EDMR Messungen zu erweitern. Auf diesem Wege wurden diverse Tests einzelner Elemente des ursprünglichen Aufbaus sowie neuer Geräte durchgeführt, um einen möglichst optimalen Aufbau zu erhalten. Ein weiteres Ziel war die Entwicklung von Mess- und Analyseprogrammen, sowie eine Automatisierung von Langzeitmessungen. Weiters wurde eine Methode zur automatischen, in-situ Kalibrierung des Magnetfeldes entwickelt, um Stabilitätsschwankungen auszugleichen.

Die Funktionalität des fertigen Messaufbaus wurde durch den Vergleich von Messungen einer Siliziumkarbid Diode mit Ergebnissen aus der Literatur demonstriert. Es zeigte sich in sämtlichen Messungen eine gute Übereinstimmung. Das Auflösungsvermögen ist hoch genug, um den Versuchsaufbau für die Chakterisierung von neuen, noch nicht untersuchten Materialien und Bauteilen heranzuziehen.

Die Arbeit wurde in Kooperation mit der KAI - Kompetenzzentrum für Automobil- und Industrieelektronik - GmbH und der Infineon Austria AG an der TU Graz realisiert. Die wesentlichen Ergebnisse dieser Arbeit wurden auf der ECSCRM 2012, der Europäischen Konferenz für Siliziumkarbid und verwandte Materialien, präsentiert.

Abstract

Defects play an important role in the reliability of semiconductor devices. The characterization and identification of defects is difficult and rising in interest for the semiconductor industries. This thesis focuses on the characterization of point defects using the electrically detected magnetic resonance (EDMR) method.

The occurrence of point defects is inevitable. Knowledge about their structure, however, offers the possibility to adapt processes for minimizing their concentration. One of the few methods to characterize point defects is EDMR. This method combines electron spin resonance (ESR) with electrical measurements and allows for the investigation of the structure of point defects in fully processed semiconductor devices. The advantage lies, on the one hand, in the ability to measure small defect concentrations and, on the other hand, in the possibility to selectively measure only a certain region of a device. This can be the depletion region of a pn-junction or the silicon-gate-oxide-interface of a MOSFET.

The goal of this study was to adapt an existing ESR setup for the measurement of EDMR. Therefore, testing of different equipment, both from the existing setup and new equipment, was performed in order to result in an optimal setup. Another target was the development of measuring and analysis software, as well as the automation of long term measurements. Furthermore, a method that allows for the automatic, in-situ calibration of the magnetic field was developed, in order to correct instabilities.

The functionality of the final setup was demonstrated by the comparison of measurements of a silicon carbide diode with a reference. All measurements were in good agreement. The resolution is high enough for the characterization of new, not yet investigated materials and devices.

The thesis was developed together with KAI - Kompetenzzentrum Automobil- und Industrieelektronik - GmbH and Infineon Austria AG at the University of Technology Graz. The main results were presented at the ECSCRM 2012, the European Conference for Silicon Carbide and Related Materials.

Acknowledgment

I would like to thank everybody who was a part of this project or has in some other way supported this thesis. I acknowledge the excellent academic supervision by Peter Hadley and Markus Koch throughout the project, which was a main reason for its success. The same applies to Gregor Pobegen and Michael Nelhiebel, who provided a lot of help from the industrial perspective. I also want to thank Thomas Aichinger for very useful hints, resulting in a fast progression of the project.

I want to express my gratitude to Wolfgang E. Ernst for enabling and supporting the project and to Günter Grampp and Georg Gescheidt-Demner for lending the ESR equipment. This work was jointly funded by the Austrian Research Promotion Agency (FFG, Project No. 831163) and the Carinthian Economic Promotion Fund (KWF, contract KWF-1521—22741—34186).

Finally, I want to thank a large number of fellow students for interesting discussions and general help on different tasks throughout the project.

Contents

Chapter I

Fundamentals

This first part of this thesis treats the fundamentals which the experiments described in the following parts are based on. It is noted that only basic concepts are given here and many derivations are excluded. More detailed descriptions of the treated subjects can be found in the cited literature.

1 Defects

Defects play an important role in the performance and reliability of semiconductor devices. Therefore, knowledge about their microscopic structure would give opportunities in avoiding them or minimizing their number by adapting the processing of devices. Various electrical measurements can reveal the presence of defects and determine their energy and density, but do not provide any information about their microscopic structure. One of these methods is deep level transient spectroscopy (DLTS) [Lan74]. Methods that can also give microscopic information are RAMAN spectroscopy, positron annihilation spectroscopy and especially electron spin resonance (ESR) spectroscopy. These methods have a finite resolution and cannot detect defects at very low concentrations. The combination of ESR with electrical measurements offers an opportunity to gain information of small total numbers of defects, particularly at interfaces in fully processed devices.

A good introduction on the importance of defects for device performance and descriptions of various detection techniques are given in the textbook *Semiconductor Material and Device Characterization* by D.K. SCHRODER [Sch06]. A collection of expertise by different authors treating various types of defects in semiconductor materials, from multiple perspectives, can be found in the textbook *Defects in Microelectronical Materials and Devices* by D.M. FLEETWOOD, S.T. PANTELIDES and R.D. SCHRIMPF [FPS09]. It includes e.g. descriptions of the structure of various defects, characterization methods, different semiconductor materials and much more. This thesis focuses on point defects and their characterization through electrically detected magnetic resonance (EDMR), beginning with an introduction of the influence defects have on semiconductors and particularly on *p*-*n* junctions.

1.1 Deep level traps

All solid materials contain defects. A theoretically ideal crystal will always contain a certain amount of point defects as a result from thermodynamics [Got07]. Real materials will, of course, show even larger numbers of defects. The basic types of point defects are displayed in Figure 1. Semiconductor fabrication and processing introduces a large number of defects. Some of these defects may have energy states within the band gap. If the states are close to the conduction or valence band they are referred to as *shallow level traps*. States that are closer to the middle of the band gap are referred to as *deep level traps*. They have a strong influence on the transitions of carriers from one band to the other, since they divide the large gap into smaller pieces and thus increase the probability of transitions. Another distinction that can be made is whether a defect behaves like a donor or an acceptor. If an impurity atom is present it is determined a donor or an acceptor depending on how many valence electrons the atom has. Donors are closer to the conduction band and acceptors are closer to the valence

band. Other types of defects such as vacancies can be donor-like or acceptor-like, depending on their charge state. Simple donor-like defects can have the charge $(+/0)$ and simple acceptor-like defects $(0/-)$.

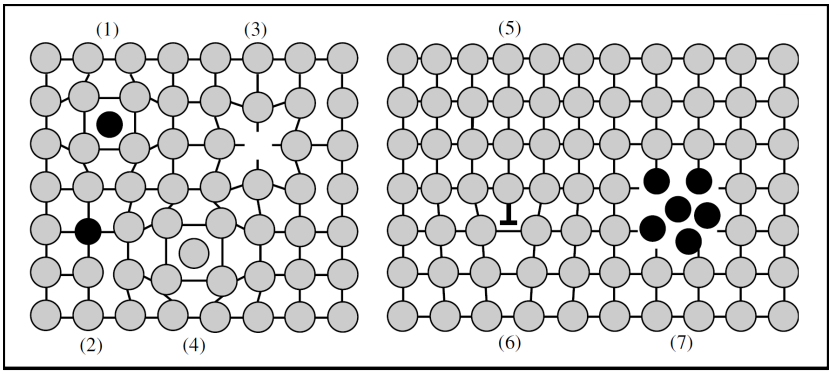

Fig. 1: The variations of point defects: foreign interstitial atoms (1), foreign substitutional atoms (2), vacancies (3), self interstitial atoms (4), stacking faults (5), edge dislocations (6) and precipitates (7) [Sch06].

As depicted in Figure 2 there are four processes possible involving charge carriers and a trap: the capture of an electron from the conduction band (a), the emission of an electron from the trap to the conduction band (b), the capture of a hole from the valence band (c), and the emission of a hole to the valence band (d). Process (d) could also be treated as an electron emission from the valence band to the trap, as indicated by the dashed arrow. However, the picture of electrons and holes is kept at this point, since it is equivalent. After process (a) either process (b) or (c) takes place, after (c) either process (d) or (a), respectively. The process (ac) where both an electron and a hole get captured by the trap is called recombination. The opposite process (bd) is the generation process where both an electron and a hole are emitted by the trap. Going forward the term generation-recombination-center (G-R-center) will be used for these defect levels. The processes (ab) and (cd) are simply trapping events where a carrier gets captured by the trap for a certain time until it is re-emitted.

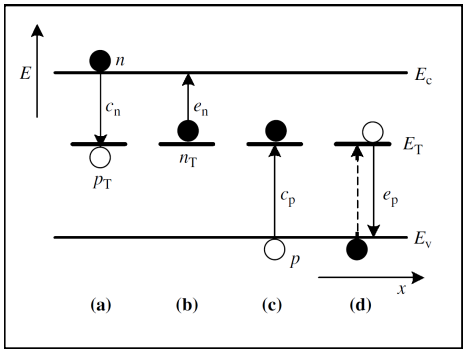

Fig. 2: Capture and emission of electrons (a,b) and holes (c,d) by a trap [Sch06].

1.2 Recombination

Recombination processes will now be discussed more closely. Despite the recombination through a *G-R*-center there is also the possibility of direct band-to-band recombination which is more probable for direct semiconductors and is not treated here.

For indirect semiconductors such as silicon (Si), germanium (Ge), or silicon carbide (SiC) the trap-assisted recombination plays a dominant role and can be described described by the SHOCKLEY-READ-HALL statistics [SR52; Hal52]. The recombination rate R is given by the equation (without derivation)

$$R = \frac{\sigma_\mathrm{n}\sigma_\mathrm{p}v_\mathrm{th}N_\mathrm{t}\left(pn - n_\mathrm{i}^2\right)}{\sigma_\mathrm{n}\left[n + n_\mathrm{i}\mathrm{e}^{\frac{E_\mathrm{t}-E_\mathrm{i}}{k_\mathrm{B}T}}\right] + \sigma_\mathrm{p}\left[p + n_\mathrm{i}\mathrm{e}^{\frac{E_\mathrm{i}-E_\mathrm{t}}{k_\mathrm{B}T}}\right]} \tag{1}$$

with σ_n and σ_p the electron and hole capture cross sections, v_th the thermal velocity of the carriers, N_t the trap density, n and p the majority carrier concentrations in the bands, n_i the intrinsic carrier concentration, E_t the trap energy, E_i the intrinsic Fermi energy, k_B the Boltzmann constant, and T the temperature. The recombination rate R, in this case, is the rate of change of the charge carrier densities per unit time.

Two conclusions immediately follow from this equation. First, the net transition rate is proportional to $\left(np - n_\mathrm{i}^2\right)$ and the sign determines whether recombination or generation is dominant. Second, the rate will be largest when $E_\mathrm{t} \approx E_\mathrm{i}$ and thus only defect levels close to the middle of the band gap are efficient *G-R*-center [SN07]. This can be understood easily when considering a defect level that is close to the conduction band after capturing an electron. The closer it is to the conduction band the more likely it will emit the electron back instead of capturing a hole. The same idea holds for holes and a defect level close to the valence band. Since the capture of both an electron and a hole is required to complete a recombination process the highest effectivity will be found when a trap is near the middle of the band gap [Gro67]. When only considering these traps the equation reduces to

$$R = \frac{\sigma_\mathrm{n}\sigma_\mathrm{p}v_\mathrm{th}N_\mathrm{t}\left(pn - n_\mathrm{i}^2\right)}{\sigma_\mathrm{n}\left(n + n_\mathrm{i}\right) + \sigma_\mathrm{p}\left(p + n_\mathrm{i}\right)} \quad . \tag{2}$$

It is interesting to understand how the energy of the trap E_t and the FERMI energies for electrons E_Fn and holes E_Fp influence the time constants of the different processes (a-d) as indicated in Figure 2. For the capture of an electron the capture time constant τ_cn is defined by the relation

$$\tau_\mathrm{cn} = \frac{1}{\sigma_\mathrm{n}v_\mathrm{th}n} \tag{3}$$

with the electron density

$$n = N_\mathrm{C}\mathrm{e}^{-\frac{E_\mathrm{C}-E_\mathrm{Fn}}{k_\mathrm{B}T}} \quad . \tag{4}$$

Here, N_C is the effective density of states in the conduction band, E_C the energy of the conduction band, and E_Fn is the FERMI energy of the electrons.

Plugging in this equation into (3) provides the equation

$$\tau_{\mathrm{cn}} \approx \frac{1}{\sigma_{\mathrm{n}} v_{\mathrm{th}} N_{\mathrm{C}}} \mathrm{e}^{\frac{E_{\mathrm{C}} - E_{\mathrm{Fn}}}{k_{\mathrm{B}} T}} \quad . \tag{5}$$

Similar calculation for hole capture results in

$$\tau_{\mathrm{cp}} \approx \frac{1}{\sigma_{\mathrm{p}} v_{\mathrm{th}} N_{\mathrm{V}}} \mathrm{e}^{\frac{E_{\mathrm{Fp}} - E_{\mathrm{V}}}{k_{\mathrm{B}} T}} \tag{6}$$

where N_{V} is the effective density of states in the valence band, E_{V} is the energy of the valence band, and E_{Fp} is the FERMI energy of the holes. Therefore, the capture time constants increase with the energy difference between the FERMI level and the band edges. Similar calculations for the emission time constants result in

$$\tau_{\mathrm{en}} \approx \frac{1}{\sigma_{\mathrm{n}} v_{\mathrm{th}} N_{\mathrm{C}}} \mathrm{e}^{\frac{E_{\mathrm{C}} - E_{\mathrm{t}}}{k_{\mathrm{B}} T}}, \quad \text{for electrons} \tag{7}$$

and

$$\tau_{\mathrm{ep}} \approx \frac{1}{\sigma_{\mathrm{p}} v_{\mathrm{th}} N_{\mathrm{V}}} \mathrm{e}^{\frac{E_{\mathrm{t}} - E_{\mathrm{V}}}{k_{\mathrm{B}} T}}, \quad \text{for holes.} \tag{8}$$

The emission time constants are, therefore, dependent on the energy spacing between the trap and the band edges [Aic07]. Equations (5) - (8) explain again, why traps near the mid-band-gap are very efficient *G-R*-center.

1.3 *p-n* junctions

It is interesting how *G-R*-centers affect the current through *p-n* junctions. The current density J_{i} through an ideal *p-n* junction is given by the SHOCKLEY equation

$$J_{\mathrm{i}} = J_0 \left[\mathrm{e}^{\frac{q_{\mathrm{e}} V}{k_{\mathrm{B}} T}} - 1 \right] \tag{9}$$

with the saturation current density J_0, the elementary charge q_{e}, and the applied voltage V. For a real *p-n* junction, recombination should be considered as well. Recalling the equation (2) under the assumptions that $E_{\mathrm{t}} = E_{\mathrm{i}}$ and $\sigma_{\mathrm{n}} = \sigma_{\mathrm{p}} = \sigma_0$, and using the relation $pn = n_{\mathrm{i}}^2 \mathrm{e}^{\frac{E_{\mathrm{Fn}} - E_{\mathrm{Fp}}}{k_{\mathrm{B}} T}}$ the result is

$$R = \frac{\sigma_0 v_{\mathrm{th}} N_{\mathrm{t}} n_{\mathrm{i}}^2 \left[\mathrm{e}^{\frac{q_{\mathrm{e}} V}{k_{\mathrm{B}} T}} - 1 \right]}{n_{\mathrm{i}} \left[\mathrm{e}^{(E_{\mathrm{Fn}} - E_{\mathrm{i}})/k_{\mathrm{B}} T} + \mathrm{e}^{(E_{\mathrm{i}} - E_{\mathrm{Fp}})/k_{\mathrm{B}} T} + 2 \right]} \quad . \tag{10}$$

For forward biasing R takes a positive value, which means that recombination is dominant, while for reverse biasing it takes a negative value and generation is dominant. The recombination current density J_{re} is obtained from the integral

$$J_{\mathrm{re}} = \int_0^{w_{\mathrm{d}}} q_{\mathrm{e}} R dx \tag{11}$$

with w_{d} being the depletion width and results without mathematical details in the equation

$$J_{\mathrm{re}} \approx \frac{q_{\mathrm{e}} w_{\mathrm{d}} n_{\mathrm{i}}}{2\tau} \mathrm{e}^{\frac{q_{\mathrm{e}} V}{2 k_{\mathrm{B}} T}} \tag{12}$$

with the carrier lifetime τ [SN07]. A more detailed derivation provides the equation

$$J_{\mathrm{re}} = \sqrt{\frac{\pi}{2}} \frac{k_{\mathrm{B}} T n_{\mathrm{i}}}{\tau F_{\mathrm{np}}} \mathrm{e}^{\frac{q_{\mathrm{e}} V}{2 k_{\mathrm{B}} T}} \tag{13}$$

with the electric field E_{np} at the location of maximum recombination which has the form

$$E_{\mathrm{np}} = \sqrt{q_{\mathrm{e}} N_{\mathrm{D}} \left(2V_{\mathrm{bi}} - V\right) / \epsilon} \quad \text{for} \quad N_{\mathrm{D}} < N_{\mathrm{A}} \tag{14}$$

and

$$E_{\mathrm{np}} = \sqrt{q_{\mathrm{e}} N_{\mathrm{A}} \left(2V_{\mathrm{bi}} - V\right) / \epsilon} \quad \text{for} \quad N_{\mathrm{D}} > N_{\mathrm{A}} \tag{15}$$

with the built in Voltage V_{bi} and the electric constant ϵ [Shu90].

The total current density is obtained by adding relation (13) to the diffusion current of an ideal *p*-*n* junction given by (9). The result can be expressed by the simple empirical equation

$$J = J_0 \left[\mathrm{e}^{\frac{q_{\mathrm{e}} V}{\eta k_{\mathrm{B}} T}} - 1\right] \tag{16}$$

with the ideality factor η [Göb11]. When the recombination current dominates, η equals 2, when diffusion dominates it equals 1, and when both currents are comparable it takes a value in between 1 and 2 [SN07]. When considering other transport mechanisms values of 4 and higher are possible [Sah62].

The EDMR method, as used in this study, is founded on the investigation of the spin dependence of recombination currents though *G*-*R*-centers. For good results it is important to operate at voltages where η is close to 2 to ensure maximum recombination and therefore large signals. As already mentioned above, only those centers located near mid-band-gap will contribute.

Before continuing with theoretical aspects of EDMR and the spin dependent recombination effect, the more fundamental method of ESR is explained in the next section.

2 Electron spin resonance

ESR spectroscopy, also known as electron paramagnetic resonance (EPR) spectroscopy, is an experimental technique used to investigate atoms and molecules with unpaired electrons. During an ESR experiment, magnetic dipole transitions are induced by electromagnetic radiation and provide characteristic information of the sample. Introductions on the fundamentals of the ESR technique are given in the textbooks *Electron paramagnetic resonance* by J.A. Weill and J.R. Bolton, as well as *Principles and applications of ESR spectroscopy* by A. Lund, M. Shiotani and S. Shimada [WB07; LSS11]. The principles presented in this section are mostly taken from these two references.

The fundamentals of ESR have been known for a long time. The splitting of energy levels in a magnetic field was first reported by P. Zeeman in 1897 and named after him [Zee97]. Today it is known that the magnetic field breaks the degeneracy of states by interacting with the different magnetic moments. The quantization of magnetic moments was observed by O. Stern and W. Gerlach in their famous experiment in 1922 [GS22]. Magnetic dipole transitions were first reported by Rabi in 1938 [Rab+38]. In 1946 F. Bloch and E.M. Purcell independently performed the first nuclear magnetic resonance (NMR) experiments of liquid and solid state materials [BHP46; PTP46]. Today NMR is a very sophisticated spectroscopy method and commonly known for its use as an imaging method in medicine.

The related ESR technique is less famous, although it has become a very powerful tool in the examination of the microstructure of atoms and molecules. It was developed even before NMR by E. Zavoisky in 1945 [Zav45a; Zav45b]. The technology to handle electromagnetic waves in the GHz range, as used in ESR experiments, was already established through the radar technology developed during World War II. Today it is a broadly used tool, especially in chemistry that allows the investigation of the electronic and geometrical structure of molecules with unpaired electrons, such as free radicals. Also semiconductors can contain unpaired electrons due to point defects, especially near interfaces e.g. in between the layers of a heterojunction, or between the substrate and the oxide layer of a metal oxide semiconductor (MOS) capacitor. ESR offers one of the few possibilities to study the structure of these defects.

2.1 Zeeman effect

Magnetic resonance spectroscopy is based on the Zeeman effect where the energies of states split according to their magnetic moments. In general, the energy E_m of a particle in a magnetic field is given by the relation

$$E_\mathrm{m} = -\boldsymbol{\mu} \cdot \mathbf{B} \tag{17}$$

where $\boldsymbol{\mu}$ is the magnetic moment vector and $\mathbf{B}$ the magnetic field vector which is aligned along the z direction. Looking at the simple, classical picture of an electron rotating around a nucleus the magnetic moment of the electron can be written

$$\boldsymbol{\mu} = -\frac{q_\mathrm{e}}{2m_\mathrm{e}}\mathbf{L} \tag{18}$$

with the electron charge q_e, the electron mass m_e and the angular momentum $\mathbf{L}$. Of course, the angular momentum is quantized and can only take discrete values that are defined by the relation

$$L = \frac{h}{2\pi}\sqrt{l(l+1)} \tag{19}$$

with the Planck constant h and the orbital angular momentum quantum number $l = 0, 1, 2, \ldots$. The projection along the z axis introduces the magnetic quantum number $m_\mathrm{l} = -l, -(l-1)..., 0, ..., l-1, l$ and leads to the relation

$$L_\mathrm{z} = \frac{h}{2\pi} m_\mathrm{l} \quad . \tag{20}$$

By plugging this relation into (17) one obtains

$$E_\mathrm{m} = \mu_\mathrm{B} B m_\mathrm{l} \tag{21}$$

with the BOHR magneton $\mu_\mathrm{B} = \frac{q_\mathrm{eh}}{4\pi m_\mathrm{e}}$. This means that the energy of the magnetic dipole in the field is split into $(2l+1)$ levels. These arguments were applied on a particle with only angular momentum. Electrons also possess a second magnetic moment caused by their spin, with the spin quantum number $s = 1/2$ and the spin projection quantum number $m_\mathrm{s} = \pm 1/2$. The energy of an electron in a magnetic field will be split due to its spin according to the relation

$$E_\mathrm{m} = g \mu_\mathrm{B} B m_\mathrm{s} \tag{22}$$

with the LANDÉ-factor g, also called g-factor or g-value. The g-factor for free electrons has been determined very precisely with good accordance to its theoretical value of roughly 2.002319 [Odo+06]. The g-factors of most bound electrons are also ≈ 2 according to theory [LSS11].

2.2 Resonance

Looking at the simple system of an electron without orbital angular momentum in a magnetic field, there are two levels due to the two possible values of m_s of $+1/2$ and $-1/2$. The energy difference between these levels derived from (22) is given by the condition

$$\Delta E = g \mu_\mathrm{B} B = h\nu \tag{23}$$

which also defines the necessary frequency ν of a photon in order to provide the energy for a transition between the levels. Equation (23) is, therefore, called the *resonance condition*. Figure 3 shows how the energy splitting depends on the magnetic field B. The g-factor can be obtained by determining the field B and the frequency ν where resonance occurs. This is usually performed by keeping the frequency constant and varying the magnetic field; the opposite procedure is also possible and fully equivalent [Mue]. When resonance occurs one observes a maximum in the absorption of the electromagnetic radiation.

Next, a closer look is taken on the process of the absorption of a photon, and the transition to the opposite spin state of an electron. Only the case of single photon absorption is considered. The magnetic moments of electrons in a magnetic field will precess around the magnetic field axis, which is also the

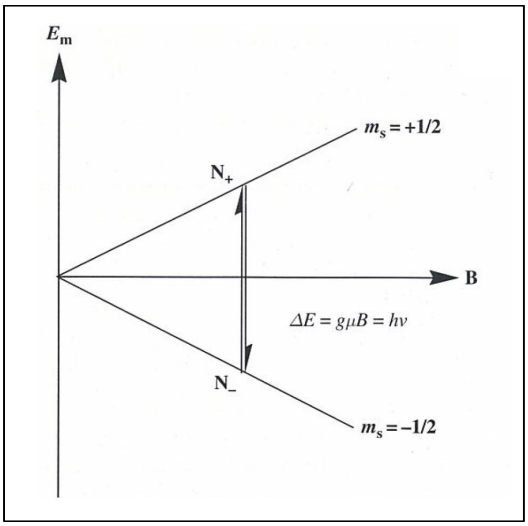

Fig. 3: Schematic of the energy splitting dependent on the magnetic field B (here $\mu = \mu_B$) [LSS11]

z axis. Figure 4 shows two cones indicating the precession of the magnetic moment vector $\boldsymbol{\mu}$. The precession will happen with the angular frequency ω_L, the so called LARMOR-frequency

$$\omega_L = g\frac{q_e}{2m_e}B = \gamma B \tag{24}$$

with $\gamma = g\frac{q_e}{2m_e}$ defined as the gyromagnetic ratio. This equation gives another expression for the frequency of a resonant photon. The picture of precessing magnetic moments also provides the resonance condition.

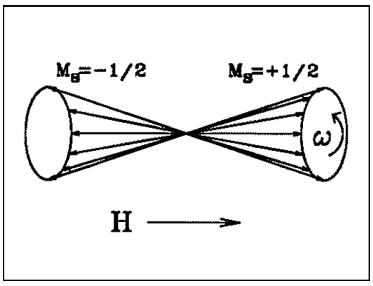

Fig. 4: Schematic of the precession cones of the magnetic moments in a magnetic field $H = \mu_0 B$ pointing in z direction [Mue].

Looking at the magnetic component of a photon that is circularly polarized in the xy-plane, with the frequency ω_L, a simple picture can be found to understand how a transition works which is called the *rotating wave approximation*. As depicted in Figure 5, the precessing magnetic moment $\boldsymbol{\mu}$ and the magnetic component of the photon $\mathbf{B}_1$ both rotate around the z axis and if $\nu = \nu_L$ the magnetic moment will "see" a static $\mathbf{B}_1$ vector. This means that now the magnetic moment will also start a precession around this "static" field vector

$\mathbf{B}_1$ which offers the possibility of a transition from one cone to the other, or in other words a spin flip.

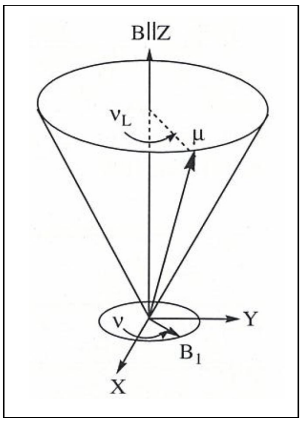

Fig. 5: Rotation of $\boldsymbol{\mu}$ and the microwave magnetic component $\mathbf{B}_1$ with the frequency $\nu_\mathrm{L} = \frac{\omega_\mathrm{L}}{2\pi}$ [LSS11].

It results from this picture that only circular polarized photons can cause transitions between the spin states. However, linear polarized radiation is a superposition of both opposite circular polarizations (and vice versa). Therefore, linear polarized light also contains photons of the proper circular polarization. It is also important that the $\mathbf{B}_1$ component of the electromagnetic field is perpendicular to the static field in order to allow transitions. Additional to this condition there is the constraint that the total angular momentum of the involved photon, plus the electron, must be conserved, which can only be fulfilled by σ-photons. Multi-photon transitions are possible, yet experiments have shown that most transitions only involve a single σ-photon [WB07]. All the conditions above can easily be fulfilled with common microwave technology, which is discussed more closely in section 4.

For spectroscopic purposes, the situation desired is when energy from the electromagnetic field is absorbed, resulting in spin transitions from the energetically lower to the higher level. This means that the higher state must have a lower occupancy than the lower state. The difference in occupation is given by the Boltzmann distribution

$$\frac{N_+}{N_-} = \mathrm{e}^{-\frac{\Delta E}{k_\mathrm{B} T}} \quad . \tag{25}$$

For this cause a large energy difference ΔE and thus a large magnetic field is favorable as well as low temperatures. Since the electromagnetic field constantly flips spins up to the higher level, at some point equal populations of the states would be reached and the absorption would stop. This, however, is not happening due to relaxation processes that try to re-establish the occupancy according to the Boltzmann distribution. The energy will be transferred to the surrounding lattice during a relaxation process, e.g. as non radiant phonons, which is macroscopically simply observed as heating of the sample.

The relaxation process will happen with a certain characteristic spin relaxation time τ_1. If the relaxation time is too slow compared to the field power some

saturation will occur due to an equilibrium between absorption and relaxation.

2.3 The g-factor

The magnetic field B appearing in the resonance condition (23) is now discussed more carefully. In general, the magnetic field that an electron experiences is not just the externally applied static magnetic field $\mathbf{B}$, but also a local field $\mathbf{B}_{\text{local}}$, caused by the magnetic moments of surrounding particles (e.g. nuclear magnetic moments). This results in an effective magnetic field

$$\mathbf{B}_{\text{eff}} = \mathbf{B} + \mathbf{B}_{\text{local}} \quad . \tag{26}$$

Therefore, the effective g-factor observed will depend on the local magnetic surrounding of the electron. Equation (26) can be rewritten as

$$\mathbf{B}_{\text{eff}} = (1 - \xi)\,\mathbf{B} = \frac{g}{g_{\text{e}}}\mathbf{B} \tag{27}$$

with ξ being the ESR equivalent to the NMR "chemical shift" and g_{e} the g-factor of the free electron. In other words, the deviation of the measured g-factor from that of the free electron will contain information of the magnetic surrounding of the electron.

It is important to note that, depending on the sample, the deviations of the g-factors can be either isotropic or anisotropic, isotropic meaning spherically symmetric. The measured spectra and their g-factors may differ in different directions with

$$g_{\text{x}} \neq g_{\text{y}} \neq g_{\text{z}} \tag{28}$$

which results in g becoming a tensor. This, in particular, applies for solid crystals where the atoms are aligned in a symmetrical pattern, while in liquids such effects are averaged out due to the movement of the molecules. The anisotropy of the g-factor can be helpful in characterizing the investigated species.

2.4 Hyperfine interaction

Hyperfine interaction occurs if the electron is located (at least partly) at atoms with nuclear spin. The orientation of the nuclear spin, with respect to that of the electron, is also quantized. This means that each state of the nucleus will deviate the effective field $\mathbf{B}_{\text{eff}}$ differently. This leads to a so-called *hyperfine splitting* of the electron spin states. The net magnetic field can have as many values as there are states of the nucleus. The energy levels of a nucleus due to its spin in the magnetic field are (similar to an electron) defined by the equation

$$E_{\text{m}} = -g_{\text{N}}\mu_{\text{N}}Bm_{\text{I}} \tag{29}$$

with the nuclear g-factor g_{N}, the nuclear magneton μ_{N} and the component of the nuclear-spin angular-momentum vector in the z direction m_{I}. The total energy of the system can be expressed by the equation

$$E(m_{\text{s}}, m_{\text{I}}) = g\mu_{\text{B}}m_{\text{s}} + a_{\text{hfs}}m_{\text{s}}m_{\text{I}} - g_{\text{N}}\mu_{\text{N}}Bm_{\text{I}} \tag{30}$$

with the hyperfine coupling constant a_{hfs} [LSS11]. Note that due to the positive charge of the nuclei the minus sign from (17) remains, in contrast to electrons. Figure 6 displays the hyperfine splitting of the electron energy levels in a hydrogen (H) atom which has a nuclear spin of $I = 1/2$ and thus $m_{\mathrm{I}} = \pm 1/2$. In this case every electron spin level splits into two levels because of the two nuclear spin states.

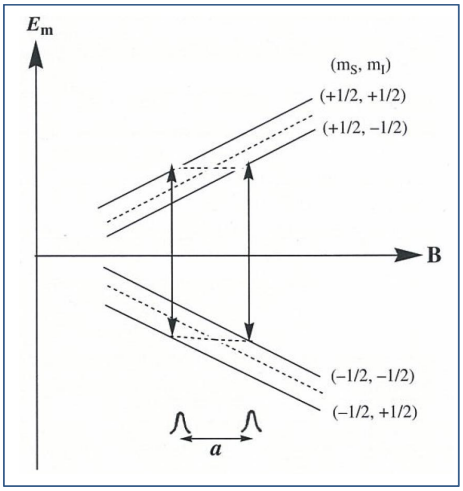

Fig. 6: Hyperfine splitting of the electron energy of an H atom in a B field [LSS11].

For experimental purposes, it is interesting to consider how many peaks to expect from a certain system, beginning with a system containing only one atom with a non zero nuclear spin I, and the number of spin levels $(2I + 1)$. The electron levels will also be split into $(2I + 1)$ levels. The possible electron spin transitions in such a system are limited by the selection rules

$$\Delta m_{\mathrm{s}} = 1 \ , \ \Delta m_{\mathrm{I}} = 0 \quad . \tag{31}$$

It is trivial that the first rule is always fulfilled for electron spin flips. The second rule is also plausible since the nuclear state should not change during an electron spin flip process. This gives the result that there are also $(2I + 1)$ possible electron transitions in ESR experiments and $(2I + 1)$ peaks to be observed. The spacing between the peaks is proportional to the hyperfine coupling constant a_{hfs} appearing in (30).

Electrons in molecules will often interact with the magnetic moments of more than one nucleus and an even more complicated hyperfine structure will occur dependent on the involved nuclei. A simple case to start with is the situation of equivalent nuclei of spin 1/2, such as H atoms in an organic compound. If an electron orbital is equally distributed over two H atoms one would observe three peaks, for three atoms one would observe four peaks and so on, which is indicated in Figure 7. The intensities given by the area under each peak are dependent on the degeneracy of the corresponding states, indicated by the arrows, and can be obtained from the Pascal triangle depicted in Figure 8 [LSS11].

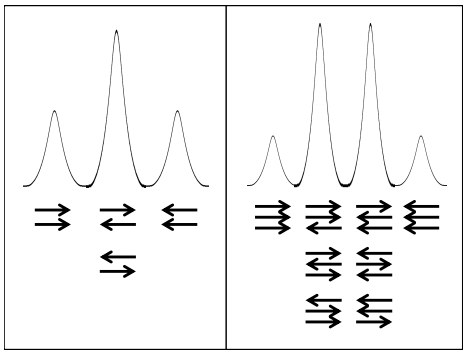

Fig. 7: Hyperfine spectrum of two (left) and three (right) equal atoms with nuclear spin 1/2.

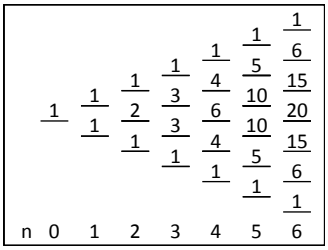

Fig. 8: The relative intensities of peaks of equal spin 1/2 atoms can be obtained from the Pascal triangle.

The case of atoms with spin 1, such as nitrogen (N), is slightly different. Here, even more degeneracies occur. One spin 1 atom will produce three equal peaks. Two spin 1 atoms, produce already five peaks with the relative intensities 1,2,3,2,1 occurring as depicted in Figure 9. Again, the degeneracy is indicated by the arrows underneath with the possible configurations of each atom $\rightarrow$, $-$ and $\leftarrow$.

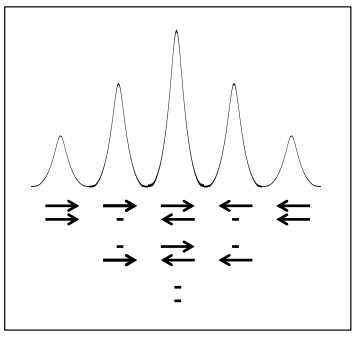

Fig. 9: Hyperfine spectrum of two equal atoms with nuclear spin 1.

All these considerations also apply to spectra containing nuclei with even higher spin. Also, different kinds of atoms can interact with the unpaired electrons. Another case would be that an electron does not have an equal probabil-

ity of presence at all interacting atoms. The relative intensities of the spectra produced by different paramagnetic species represent their concentrations in a sample [WB07].

Additionally, for elements that do not possess nuclear spin, there may be isotopes with non-zero nuclear spin existing. If an unpaired electron is bound to atoms of such elements the spectrum can contain hyperfine peaks with a relative intensity according to the natural occurrence of the isotopes.

The last point concerning hyperfine interaction that will be discussed here are some aspects about its isotropy. As already mentioned in section 2.3 anisotropies can be observed for certain species, especially for solids where they cannot be averaged out due to molecular movements. It is necessary to distinguish between the two cases, isotropic and anisotropic coupling.

Isotropic coupling

Isotropic coupling occurs for electrons with a finite probability of presence at the nucleus, or with other words, electrons in an s-orbital. This case is referred to as *contact coupling*. The hyperfine constant can be calculated according to Fermi using the equation

$$a_{\mathrm{hfs}} = \frac{2}{3}\mu_0 g \mu_{\mathrm{B}} g_{\mathrm{N}} \mu_{\mathrm{N}} \rho\left(X_{\mathrm{N}}\right) \tag{32}$$

where $\rho\left(X_{\mathrm{N}}\right)$ is the unpaired electron density at a nucleus located at X_{N} and μ_0 the magnetic field constant [LSS11]. This means that the hyperfine coupling constant a_{hfs} is directly proportional to the electron density $\rho\left(X_{\mathrm{N}}\right)$ which is related to the electronic structure of the molecule.

Anisotropic coupling

For unpaired electrons localized in p-, d- or f-orbitals the situation is different since orbitals are not spherically symmetrical. This results in an anisotropic hyperfine coupling, dependent on the orientation of the orbital in the magnetic field. The hyperfine coupling constant is referred to as B_{hfs} and can significantly vary in different directions e.g. for a 2p orbital it varies from $B_{\mathrm{hfs,z}} = 2B^0_{\mathrm{hfs}}$ to $B_{\mathrm{hfs,x}} = B_{\mathrm{hfs,y}} = -B^0_{\mathrm{hfs}}$ [LSS11].

There is also some "fine structure" or "zero-field splitting" occurring in systems containing a total electron spin of 1 or higher. This can be the case for free radicals with a small spacing in-between, or for transition metal ions that contain several semi-occupied shells [LSS11]. For this study, this effect is of little interest and will be left out.

2.5 Detectable species

For the investigation of bound electrons it is important that only species with semi-occupied orbitals are detectable. If an orbital is filled, the two electrons will have opposite spins and the total magnetic moment will be zero. Therefore, only an unpaired electron will have a magnetic moment that can interact with the magnetic field. Despite this limitation there is a wide range of situations where electrons are found unpaired and give an ESR response.

Free radicals

Free radicals are atoms and molecules that have an unpaired valence electron. These substances are, in general, very reactive but there are also some stable ones including diatomic oxygen (O_2), nitric oxide (NO), nitrous oxide (NO_2) and chlorine dioxide (ClO_2) [Mue]. Free radicals often occur as intermediate products in chemical reactions and can, under some conditions, have sufficient lifetimes to be observed [LSS11]. Also large organic molecules may contain unpaired delocalized electrons. Free radicals can also be the result of radiation damage caused by high energy particles like x-rays or gamma rays. Chemical bonds in biological systems can be broken by the high energy photons which produce free radicals that can be harmful to the organism [Mue].

Transition metal ions

Transition metals have semi-occupied valence shells. They can contain up to six unpaired electrons and give rise to spectra with split energy levels.

Point defects in solids

Solid crystals often contain defects that can capture an electron and be detected. An example is the E′ center in silicon dioxide (SiO_2). Defects in semiconductor crystals are treated in section 1.

Triplet state molecules

Some molecules can be excited into a triplet state e.g by light illumination. These systems then contain two unbound electrons with a total spin of s=1 and strongly interact with each other. They can usually be studied in single crystals or glasses [LSS11].

Biradicals

In biradicals the distance between the unpaired electrons is larger and the interaction weak. These systems behave as two weakly interacting radicals [WB07].

Ions on helium (He)-nanodroplets

A sophisticated method that allows for ESR spectroscopy of isolated ions has been demonstrated by M.Koch *et al.* [Koc09]. The ions are placed on superfluid He-nanodroplets where they can be examined under stable conditions.

2.6 Line broadening effects

For positive results good resolution is desired. As in all spectroscopic techniques, line broadening will affect the the quality of spectra. Distinguishing between heterogeneous and homogeneous broadening must be established first. Heterogeneous broadening is broadening due to an overlap of spectra with different center lines. Homogeneous broadening is due to overlap of lines with the same center frequency but different line widths.

Heterogeneous broadening

Heterogeneous broadening is often due to experimental apparatus effects. This is, for instance, the inhomogeneity of the static B field. Not all atoms in a sample will experience the same magnetic field and will come in resonance at a different applied field, which results in a broadened spectrum. Another heterogeneous broadening effect lies in unresolved hyperfine structures. An example is the stable free radical 2,2-diphenyl-1-picrylhydrazyl (DPPH) where the unpaired electrons have a strong interaction with two N atoms giving rise to five lines. However, there are three more N atoms and twelve H atoms that cause additional 10^5 lines that, of course, cannot be resolved and therefore lead to some heterogeneous broadening [Mue]. Heterogeneous broadening results in a Gaussian line shape.

Homogeneous broadening

Besides the natural line width that comes from the uncertainty principle, there are basically two characteristic times τ_1 and τ_2 that lead to homogeneous broadening. τ_1 has already been introduced in section 2.2 as the spin relaxation time. It is characteristic for the time scale of the spin flipping processes and leads to a Lorentzian line shape of $1/\tau_1$. The other time constant τ_2 is the so called phase relaxation time.

Returning to the picture of the possible states rotating in cones around the z axis, τ_1 would be the time that a spin would remain in one cone before spontaneously flipping over to the other one. This time is strongly influenced by collisions where energy is exchanged. In liquids and especially in solids, τ_1 dominates by far.

During the process of a resonant spin flip some time dependent fluctuation can occur and interrupt the process. The spin will remain at a different position on the same cone without exchange of energy. It will be dephased and τ_2 is related to this dephasing, and therefore called phase relaxation time. One process that plays a major role for τ_2 broadening is spin exchange. If during a collision process two electrons change their spins the total energy will not change, but since both electrons flip into opposite cones, the phase of their spin functions will be interrupted. If the total spin orientation changes during a collision it will affect τ_1. [Mue].

Another aspect that should considered is power broadening. If the microwave power extends a certain level, stimulated emission will start playing a role in the relaxation processes and reduce the lifetime to a shorter value than τ_1, which leads to additional broadening. It is important to operate at powers below this limit.

2.7 Summary

ESR is an experimental method that offers the possibility for insight into atomic and molecular structure, complementary to other methods. The informations one can obtain from an ESR spectrum are summarized in the following.

The g-factor which is characteristic for each spin system. It is determined by the magnetic field of a line with the known microwave frequency from (30).

Hyperfine splitting contains information of the environment of an unpaired electron. The number of peaks in a hyperfine spectrum is determined by the

interactions of the nuclear magnetic moments with the electron. The number of peaks and relative intensities give a clue to the number of nuclei involved, their nuclear spins, as well as their concentrations. Besides atoms like H, N or halogens there are also rare isotopes of other atoms that have a non-zero nuclear spin and produce hyperfine splittings according to their concentrations in a sample. The spacing between hyperfine peaks of the same electron spin is proportional to the hyperfine constant a_{hfs} for isotropic and B_{hfs} for anisotropic interaction.

The isotropy of the spin system tells about the character of the electron orbitals. Only s-orbitals are isotropic while p-, d- and f-orbitals are anisotropic. Both the hyperfine splitting as well as the g-factor can change with the orientation of the sample and give information about the s-character of an orbital.

Among these static properties one can also observe dynamic properties, like the change in ESR response of the sample during an annealing process. In a solid, defects play a large role in the generation of ESR spectra, and annealing can produce or heal defects, which can be observed.

There are lots of applications of ESR spectroscopy and more sophisticated methods that are based on ESR have been developed, including electron nuclear double-resonance (ENDOR), pulsed ESR, or electron spin echo modulation (ESEEM) [LSS11]. This study focuses on ESR combined with electrical measurements which is explained in the following section.

3 Electrically detected magnetic resonance

EDMR describes all types of experiments where the electron spin resonance of a sample, in a magnetic field, is observed through an electrical measurement. Various transport mechanisms such as recombination, trapping, tunneling or scattering can be spin dependent [Lo11]. This section will focus on spin dependent recombination (SDR) in diodes, where, the resonant change of the recombination current through the depletion regions of p-n-junctions is observed. The SDR effect was first explained in 1970 by Lépine who also proposed a model to quantitatively describe its magnitude [LP70; Lép72]. The experimental results, however, revealed a much larger effect than expected by the Lépine model [SBK77]. Thus, a different model was proposed by Kaplan, Solomon and Mott in 1978 [KSM78]. This model predicts the measurable effect very well. However, it was shown by B. Stich *et al.* that some more specifications might be necessary, which they included in their model [SGS95]. All three models are introduced at this section in order to provide an optimal perspective on the spin dependent recombination effect.

3.1 The Lépine Model

The first model which explained the spin dependent recombination effect was proposed by Lépine [Lép72]. The idea was that the spin dependence is due to the polarization of the electron and hole spins. Even though it is not quantitatively in agreement with experiments, this model gives a simple picture of how the process can be imagined. Figure 10 depicts how an electron uses a trap to recombine from the conduction band to the valence band. This recombination process is also described in section 1.1.

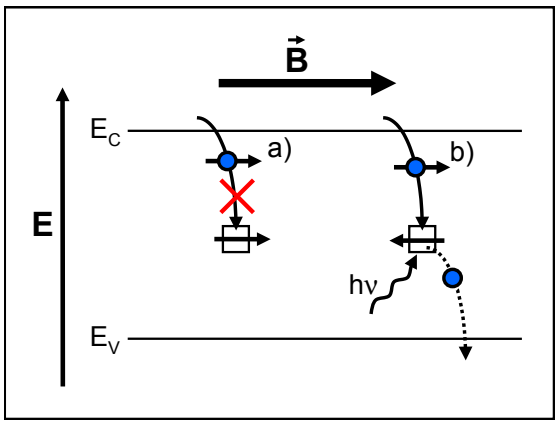

Fig. 10: Schematic image of the spin dependent recombination process according to Lépine [Lép72]. **B** indicates the direction of the magnetic field that polarizes the spins. For an electron with equal spin as the trap, the recombination is blocked due to Pauli exclusion principle a); a resonant photon can flip the spin and make the transition possible b).

The spin dependence is obvious when looking at the spins of both the electron and the G-R-center. If the spins are polarized in the same direction the

recombination through the trap is blocked due to the PAULI exclusion principle, while for opposite spins the recombination through the trap is possible. Resonant photons can cause spin flips. Therefore, the measurable effect proposed by this model lies in the polarization of the electron and the trap. The capture cross section Σ for the electron being trapped by the G-R-center is given by the equation

$$\Sigma = \Sigma_0 \left(1 - p_\mathrm{e} p_\mathrm{h}\right) \tag{33}$$

with p_e and p_h being the polarizations of the electron and trap respectively. The maximum measurable relative current change is

$$\frac{\Delta J}{J} = \frac{\Delta \Sigma}{\Sigma} = p_\mathrm{e} p_\mathrm{h} \tag{34}$$

which has the order 10^{-6} at room temperature in a field of $B = 3000\,\mathrm{G}$ [KSM78]. Several experiments have revealed a larger effect, of orders of magnitude [Lép72; Sol76; SBK77; LTK77]. Therefore, the LÉPINE model, although giving a picture that is easy to understand, is not capable of quantitatively explaining the effect. For this reason, a more sophisticated model was developed by KAPLAN *et al.*

3.2 The Kaplan-Solomon-Mott model

The KAPLAN-SOLOMON-MOTT (KSM) model starts from the perspective that the origin of the SDR effect does not lie in the magnetic field polarization since it cannot explain the order of magnitude of the signal[KSM78]. The formation of an intermediate pair-state prior to recombination is introduced, which explains the departure from isotropy without the applied magnetic field. This pair-state is formed by an electron and a hole in proximity where they can either recombine or dissociate. This pair can either have opposite (singlet) or equal (triplet) spin orientation. Only the singlet state can recombine due to spin conservation ($\Delta S \stackrel{!}{=} 0$).

Due to the recombination the singlets are assumed to have a shorter lifetime and will have a smaller steady-state population than the triplets. By saturating the spin system under resonant conditions this difference in population can be evened out. The increased population of singlets under resonance results in a rise in the recombination rate.

The recombination probability $W_\mathrm{R}(\theta)$ of a spin pair with angle θ in between is

$$W_\mathrm{R}(\theta) = W_\mathrm{S} \frac{1 - \cos\theta}{4} \tag{35}$$

with the recombination rate for a pure singlet pair W_S. The steady-state density $N(\theta)$ of pairs with angle θ is given by the expression

$$N(\theta) = \frac{c(\theta)}{W_\mathrm{R}(\theta) + W_\mathrm{D}} \tag{36}$$

with the dissociation probability W_D and the creation rate of pairs $c(\theta)$ which takes the form

$$c(\theta) = \frac{C}{2} \sin\theta \tag{37}$$

where C is the total creation rate, depending on the injected carrier densities n and p. By plugging in, one obtains for the steady-state density of pairs

$$N(\theta) = \frac{2C\sin\theta}{4W_{\mathrm{D}} + W_{\mathrm{S}}(1-\cos\theta)} \quad . \tag{38}$$

If through resonance a random distribution is established, the recombination probability will be just $W_{\mathrm{R}} = W_{\mathrm{S}}/4$ and the steady state density of pairs $N_{\mathrm{Sat}}(\theta)$ becomes

$$N_{\mathrm{Sat}}(\theta) = \frac{2C\sin\theta}{4W_{\mathrm{D}} + W_{\mathrm{S}}} \quad . \tag{39}$$

The recombination rates R for both cases are obtained by solving the integral $R = \int_0^\pi N(\theta) W_{\mathrm{R}}(\theta)\, d\theta$ and the relative change becomes

$$\frac{\Delta R}{R} = \frac{R - R_{\mathrm{Sat}}}{R} = 1 - \frac{1}{(1+4\lambda)\left(1 - 2\lambda\log\frac{1+2\lambda}{2\lambda}\right)} \tag{40}$$

with the saturated recombination rate R_{Sat} and $\lambda = W_{\mathrm{D}}/W_{\mathrm{S}}$. The order of magnitude of $\Delta R/R$ is above 10^{-4} for a wide range of λ and is in good agreement with experiments [KSM78]. Additionally, there is no dependence on the magnetic field, and experiments have shown that indeed the order of magnitude is similar for different microwave frequencies [KSM78].

What is not treated explicitly in this model is the nature of the formed pair. It is only assumed to be an electron and a hole in proximity which also includes the case where both of them are captured in the same trap. The work by Stich *et al.* however revealed that a pair of two traps seems to be required for SDR processes.

3.3 The model of Stich *et al.*

EDMR measurements on phosphorus (P) doped Si only showed the expected response when a second dopant level introduced by boron (B) doping was present [SGS95]. From this observation a model was developed that includes an uncharged, exchange coupled donor-acceptor pair ($\mathrm{D^0A^0}$ pair) in the recombination process.

The time dependence of the concentration of electrons in the conduction band, with a simplified donor-acceptor model where capture and emission of carriers by acceptors and donors are neglected, is given by the equation

$$\frac{dn}{dt} = g_0 - W_{\mathrm{R}} n \tag{41}$$

with g_0 the generation rate of charge carriers and W_{R} the recombination probability determined by the $\mathrm{D^0A^0}$ pair recombination process. For a steady-state the signal S_{EDMR} is given by the proportionality

$$S_{\mathrm{EDMR}} = -n\frac{\Delta W_{\mathrm{R}}}{W_{\mathrm{R}}} \quad . \tag{42}$$

The different configurations of the $\mathrm{D^0A^0}$ pair can have total spin $m_{\mathrm{s}} = -1, 0, 1$ and have the occupancies N_{-1}, N_0 and N_1. Similar to the idea in the KSM model, the recombination rates of the $m_{\mathrm{s}} = 0$ states are much higher

and the steady-state occupancy N_0 much smaller than N_{-1} and N_1. With the transition probability W_{ESR} and the dissociation probability W_{D}, as well as the generation probability G, the rate equations

$$\frac{dN_{\mathrm{i}}}{dt} = G\left(n - \sum_{j=-1}^{+1} N_{\mathrm{i}}\right) - N_{\mathrm{i}}\left(W_{\mathrm{ESR}} + W_{\mathrm{D}} + W_{\mathrm{R}}^{i}\right) + \sum_{j\neq i} N_{\mathrm{i}} W_{\mathrm{ESR}} \tag{43}$$

are found. Assuming the simplest case where $W_{\mathrm{R}}^{1} = W_{\mathrm{R}}^{-1} = 0$ and $W_{\mathrm{D}} = 0$ one can obtain the stationary solution for the EDMR signal

$$S_{\mathrm{EDMR}} \propto K \frac{W_{\mathrm{ESR}} T_{\mathrm{R}}}{1 + W_{\mathrm{ESR}} T_{\mathrm{R}}} \tag{44}$$

with $K = \frac{2GN}{4G+W_{\mathrm{R}}^{0}}$ and $T_{\mathrm{R}} = \frac{4G+W_{\mathrm{R}}^{0}}{GW_{\mathrm{R}}^{0}}$. Equation (44) agrees with the shape of saturation curves experimentally determined by measurements at different microwave powers P_{MW}, assuming that $W_{\mathrm{ESR}} \propto P_{\mathrm{MW}}$. The form of the equation does not change, even when including spin-lattice relaxation or $W_{\mathrm{D}} \neq 0$. Only the expressions for K and T_{R} would become more complicated [SGS95]. The derived power dependence is similar, as in optically detected magnetic resonance (ODMR) experiments that are based on an acceptor-donor pair recombination mechanism [Spa98]. This hints that the SDR effect may indeed be founded on recombination through a $\mathrm{D}^0\mathrm{A}^0$ pair.

3.4 Summary

The method of EDMR is a powerful tool for the investigation of traps in semiconductor devices. Its has several advantages, compared to conventional ESR.

First, the defect concentration can be much lower. The detection limit for ESR experiments lies in the range of 10^{10} spins [LSS11]. When investigating defects at an interface in a semiconductor, the total number of defects may lie close to or below this limit but EDMR experiments can still detect them with good signal-to-noise ratio (SNR).

Second, EDMR is a more selective technique than ESR. A fully processed device will contain many different defects in different layers and interfaces. Since conventional ESR is measured in the absorption of the sample as a whole it does not contain information about whether the defects detected are in the region of interest. This is contrary for EDMR. The response is measured from the current and it can be selected very precisely where the current flows in the device. This offers a good opportunity to measure only the region of interest of a device.

Third, it gives advantages when investigating the evolution of the defects and their spectra after stress. This can be current, voltage, or also thermal stress. The advantage here is that the stress can be applied without taking the sample out of the cavity, since it is already electrically connected. Especially for thermal stress, it can be beneficial to include a heating possibility on the device by intelligent chip design.

EDMR has been used in the past to characterize the Si-SiO_2 interface (e.g. [ML00]) and is rising in interest for the characterization of new materials, both inorganic and organic.

4 Microwaves

For ESR and EDMR experiments usually magnetic fields of roughly 3000 G are used which, according to (23), corresponds to microwaves of the X-band regime ($\nu \approx 10^4$ MHz). Part of this study focuses testing of a microwave source, as well as different resonant cavities.

A very detailed theoretical description of a all technological elements used in ESR spectroscopy is given in the textbook *Electron Spin Resonance - A Comprehensive Treatise on Experimental Techniques* by C.P. Poole [Poo96]. This section only focuses on the generation and guidance of microwaves, as well as resonant cavities, and the field distributions resulting from electrodynamics. Additional detailed information can be obtained from the book.

4.1 Reflex klystrons

Reflex klystrons are microwave generators that are largely used in ESR spectroscopy. The generation mechanism lies in electrons that are emitted by a cathode and accelerated before crossing a resonator (cavity) through a gap. There they are divided into bunches due to radio frequency (RF) electromagnetic fields in the gap. The bunches propagate over a certain drift space before being reflected back by a negatively charged plate. They re-enter the cavity after a certain time defined by the voltage of the reflector. If the reflection voltage and, therefore, the time of flight is set properly, they will be debunched while crossing the gap. This way, energy is transferred into the RF field which is then amplified and the reflex klystron can oscillate. The constraints are that the beam-current must be sufficient to compensate losses, and the acceleration voltage and the reflection voltage must be in accordance. The oscillating RF field can then be coupled out of the cavity and used for experiments.

It is usually desired to change the frequency of the electromagnetic waves that are generated, which requires tuning of the klystron cavity. This is, on the one hand, attained by changing the resonant frequency of the resonator by changing its length (mechanical tuning) and, on the other hand, by changing the reflection voltage (electrical tuning). Often klystrons are operated with a sawtooth reflection voltage, which results in an output signal that scans a small frequency range during every sawtooth period. This mode is often used to match the output frequency with the resonance frequency of the load, as depicted in Figure 11.

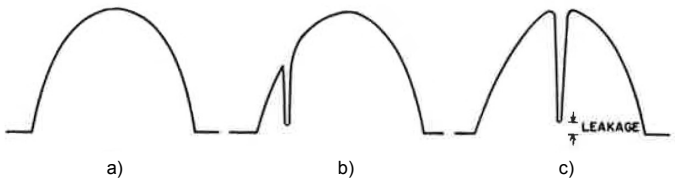

Fig. 11: Klystron in scan mode: a) Power dependence of the frequency; b) Changing the length of the klystron cavity is used to find the resonant frequency of the load; c) optimal coupling to the load with reflected power (leakage) [Poo96].

Klystrons that are used for spectroscopic purposes are operated in a mode where the frequency is constant. A system to automatically stabilize ν can be included in the microwave bridge. If changes in the frequency occur the reflector voltage is adapted so that it corrects the frequency. This mode is called automatic frequency-controll (AFC).

4.2 Waveguides

The microwaves that are generated by the source, as described in the past section, are guided in different ways. Coaxial lines may be used, however, they have an attenuation of roughly 0.7 dB/m for microwaves of the X-band regime ($\nu = 10^4$ MHz) [Poo96]. This is why low-loss waveguides are used when possible. Microwaves in the X-band range can easily be guided by rectangular waveguides with dimensions of a couple centimeters.

The modes and frequencies that can spread in a waveguide can be derived from the Maxwell equations

$$\nabla \times \mathbf{E} = -\frac{\partial \mathbf{B}}{\partial t} \tag{45}$$

with the electric field vector $\mathbf{E}$, the magnetic flux density vector $\mathbf{B}$ and time t and

$$\nabla \times \mathbf{H} = \mathbf{J} + \frac{\partial \mathbf{D}}{\partial t} \quad . \tag{46}$$

with the magnetic field vector $\mathbf{H}$, the current density vector $\mathbf{J}$ and the displacement vector $\mathbf{D}$.

There are different modes that can propagate along microwave transmission lines which are the transverse electromagnetic mode (TEM), the transverse electric mode (TE) and the transverse magnetic mode (TM). These modes are defined by the following conditions for their electric and magnetic field component in the direction of propagation z_{MW}

$$H_{\mathrm{z}} = 0,\ E_{\mathrm{z}} = 0 \quad \mathrm{TEM} \tag{47}$$

$$H_{\mathrm{z}} \neq 0,\ E_{\mathrm{z}} = 0 \quad \mathrm{TE} \tag{48}$$

$$H_{\mathrm{z}} = 0,\ E_{\mathrm{z}} \neq 0 \quad \mathrm{TM}. \tag{49}$$

The general boundary conditions for the field components in a waveguide, that consists of ideally conducting walls, are that the electric field must be perpendicular to the wall and the magnetic field parallel, respectively. This cannot be fulfilled by TEM waves and thus, only TE and TM waves can propagate in a rectangular waveguide. The calculations for the field distributions of plane waves are straight forward and can be found in the text by Poole [Poo96]. The field distributions for different modes are depicted in Figures 12 and 13.

The limit of frequencies that can propagate in a waveguide with the dimensions a and b is interesting for experimental purposes. The minimum frequency that can propagate is given by the equation

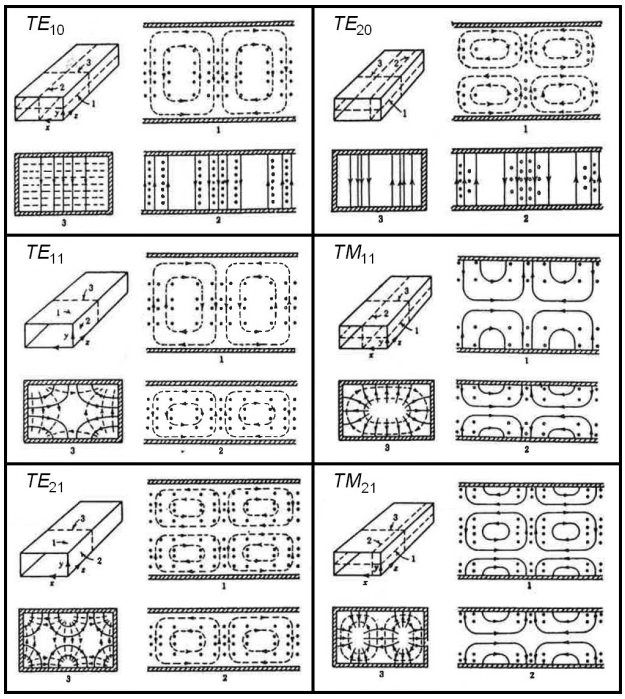

Fig. 12: Twodimensional field distributions for different modes in rectangular waveguides [Poo96].

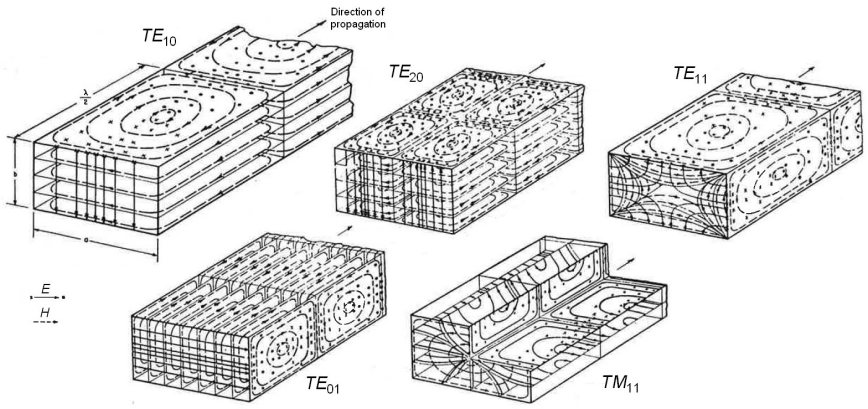

Fig. 13: Threedimensional field distributions for different modes in rectangular waveguides [Poo96].

$$\nu_{\mathrm{ij}} = \frac{c}{2}\sqrt{\left(\frac{i}{a}\right)^2 + \left(\frac{j}{b}\right)^2} \tag{50}$$

where c is the speed of light. For $a > b$ this frequency is ν_{10}. The mode with the smallest propagable frequency for $a > b$ is the TE_{10} mode and the equation

$$\nu_{\mathrm{TE}} = \nu_{10} = \frac{c}{2a} \tag{51}$$

defines its frequency ν_{TE} [KR09].

4.3 Transversal electric field cavities

For ESR and especially EDMR experiments it is desired to have high powers in order to saturate the spin systems. Microwave bridges are limited in power but by performing the experiment in a resonator (cavity) one can achieve much higher powers. The electromagnetic field calculations for rectangular cavities are similar to those for waveguides with the difference of confinement in one more dimension. The calculations give the resonant frequency ν_0 for rectangular $\mathrm{TE}_{\mathrm{ijm}}$ cavities of

$$\nu_0 = \frac{c}{2}\sqrt{\left(\frac{i}{a}\right)^2 + \left(\frac{j}{b}\right)^2 + \left(\frac{m}{d}\right)^2} \tag{52}$$

where a, b and d are the dimensions of the cavity [Poo96]. It is suitable to use $\mathrm{TE}_{10\mathrm{m}}$ cavities for ESR and EDMR experiments (with $m \geq 2$). As depicted in Figure 14, a TE_{102} cavity contains a plane of maximum B and minimum E at $z_{\mathrm{MW}} = d/2$. Generally in $\mathrm{TE}_{10\mathrm{m}}$ cavities there are $m - 1$ of these planes. They are ideal positions to place specimens since the resonance mechanism only uses the B field. Additionally electrical measurements are less influenced due to the minimum of the electric field.

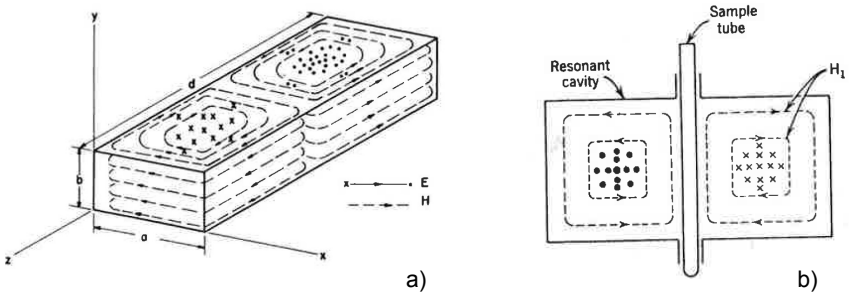

Fig. 14: a) Field distribution in a TE_{102} cavity; b) Position to place a specimen at $H = \max; E = \min$ [Poo96].

Q factor

A quantity that describes the quality of a resonator is the Q-factor or simply Q. The Q describes how much power P_{cavity} can be present in a cavity, compared

to the losses. Under steady-state conditions the losses are equal to the input power P_{input}. It can be determined from the shape of the absorption peak of the resonator, which is shown in Figure 11 c). Q is defined as the quotient of the resonant frequency ν_0 and the full width at half maximum ν_{FWHM} of the absorption peak

$$Q = \frac{P_{\mathrm{cavity}}}{P_{\mathrm{input}}} = \frac{\nu_0}{\nu_{\mathrm{FWHM}}} \quad . \tag{53}$$

The theoretical value for the Q of an unloaded $\mathrm{TE_{i0m}}$ cavity is given by the equation

$$Q_{\mathrm{u}} = \frac{\lambda}{\delta} \frac{(abd/2\pi)\left(k_{\mathrm{x}}^2 + k_{\mathrm{z}}^2\right)^{3/2}}{k_{\mathrm{x}}^2 d\,(a+2b) + k_{\mathrm{z}}^2 a\,(d+2b)} \tag{54}$$

with $k_{\mathrm{x}} = \frac{\pi i}{a}$, $k_{\mathrm{z}} = \frac{\pi m}{d}$. The skin depth δ appearing in this equation is

$$\delta = \sqrt{\frac{2}{\omega \mu_0 \mu_{\mathrm{r}} \sigma_0}} \tag{55}$$

with the angular frequency ω, the magnetic field constant μ_0, the relative permeability μ_{r}, and the conductivity σ. Thus, cavities plated with a high conducting material such as silver (Ag) can reach higher Q factors.

5 Lock-in-amplification

The output signal $\frac{\Delta J}{J}$, whether in ESR or EDMR experiments, is very small and contaminated with noise. For this reason, amplification and noise filtering is needed. This is obtained by lock-in-amplification. The output signal is dependent on the magnetic field B. By modulating the magnetic field with a small alternating signal with amplitude B_{mod} and frequency f_{mod} the output signal is also modulated. This way the output signal is made periodic and frequency filtering can be applied, which results in noise reduction.

This is attained by using a phase detector [HH89]. The output signal is multiplied with a rectangular alternating current (AC) signal of the same frequency and integrated with a low pass filter. Often the signal to generate B_{mod} is also used as reference signal. The result is a direct current (DC) signal that is dependent on the phase difference between the reference and the output signal. The time constant of the low-pass filter τ_{LP} defines how many periods of the output signal are integrated. Since the noise has a wide range of frequencies a large part is averaged out. The higher τ_{LP} the narrower is the bandwidth of frequencies close to f_{mod} and the higher the SNR. For good results the time constant should be at least five modulation periods. Since the time constant is related to the waiting time per measurement point it has a large influence on the total scan time.

Of course, it would be possible to perform a very long and slow scan. However, the experimental setup can drift on long time scales due to ambient temperature changes. Therefore, it is favorable to perform time averaging by averaging multiple shorter scans.

Also for the modulation amplitude B_{mod} an optimum has to be found. The larger the amplitude the better the lock-in-amplification works. However, if B_{mod} is in the range of the peak-widths of the spectrum broadening of the lines will occur. Therefore, it should be chosen smaller than the peaks to be resolved, but big enough to get sufficient modulation of the signal. The empirical equation

$$t_{\mathrm{scan}} B_{\mathrm{mod}} = 5\tau_{\mathrm{LP}} \Delta B_{\mathrm{scan}} \tag{56}$$

gives guidance in optimizing the measuring parameters dependent on the total scan time t_{scan} and the scan range ΔB_{scan} [Aic11]. Of course, the optimal parameters are dependent on the setup, as well as the examined sample, and thus a good set of parameters for one system may not work for a different one.

Chapter II

Experimentals

This chapter gives detailed descriptions of the experimental setup that was built around a commercial *Varian E9* ESR spectrometer. The focus will lie on the adaptions that were necessary in order to perform EDMR measurements, and on ideas to improve the SNR and the accuracy of the recordings. First, the developed setup as a whole, including the idea how a measurement is performed is described. Next, a detailed description of the most important parts of the setup and factors that have an influence on their performance are treated.

6 General description of the experimental setup

The setup is displayed in the schematic in Figure 15. Black lines connecting devices mark signal lines where the arrows indicate the direction of a signal. The basic measuring principle lies in the measurement of the response of a sample exposed to both a quasi-static magnetic field and resonant microwave photons. Quasi-static, in this case, means that the magnetic field is held constant for every measurement point during a sweep.

The microwaves are generated by a microwave bridge and are directed to a resonant cavity (C) via a waveguide (A). The frequency is locked to the resonance frequency of the cavity in order to minimize reflections and maximize the power that is injected into the cavity. In order to get a precise frequency measurement, 10% of the power generated by the microwave source is picked up by a directional coupler (B), and collected by a diode. This signal is used by a frequency counter to determine the frequency with high accuracy.

The quasi-static magnetic field is generated by the electromagnets (D). In order to record a spectrum, the magnetic field is swept, while the microwave frequency must stay locked to the resonance frequency of the cavity. The sweep is controlled by a computer using a digital-to-analog-converter (DAC) that is connected to the power supply of the magnet. The corresponding B-field is the abscissa of a measurement.

The response of the sample, whether in ESR or in EDMR experiments, is small in comparison to noise. For this reason lock-in-amplification is used. Therefore, the magnetic field is modulated with the modulation coils (E) and only responses with the modulation frequency are amplified by the lock-in-amplifiers. The modulation coils are driven by the internal oscillator of a lock-in-amp. The cavity has two positions for a specimen (I & II) which is described in more detail in section 9. In addition to investigating either an ESR sample or an EDMR sample, it offers the possibility to examine both simultaneously.

The response of an ESR sample is measured in the signal reflected by the cavity. The microwave source contains a measuring unit that gives out a signal proportional to the reflected power. Thus, when a sample comes in resonance more power is absorbed and the output signal changes. Due to the modulation, the ESR signal will oscillate with the same frequency and can be amplified by one of the lock-in-amps. With an analog-to-digital-converter (ADC) the response to the applied magnetic field is sent back to the computer and gives the ordinate axis of a spectrum.

The lock-in-amplification and recording of the spectrum is equivalent when performing an EDMR measurement. The difference lies in the generation and measurement of the response, which is completely electrical. In the simplest case, a diode is forward biased by a current amplifier that also measures and

pre-amplifies the current through the diode. When in resonance, the current changes due to enhanced recombination rates, as described in section 3. This signal is again modulated and can be amplified by a lock-in-amplifier.

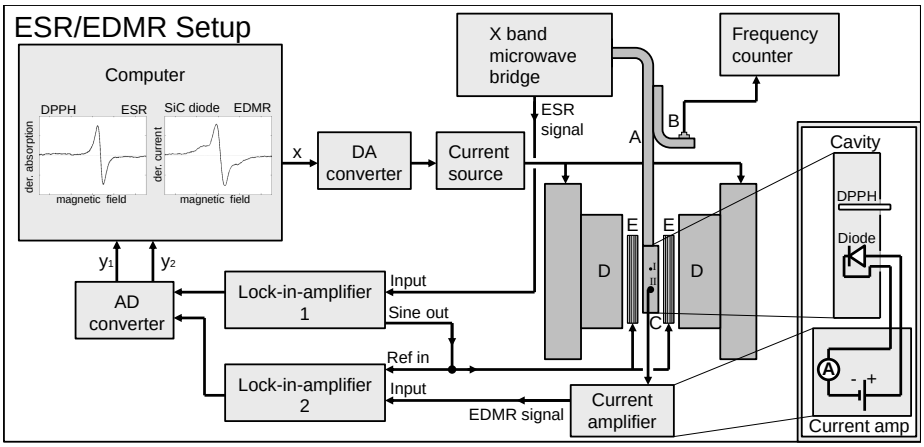

Fig. 15: Schematic drawing of the experimental setup.

As previously mentioned, this setup allows the measurement of the ESR signal of a standard, in this study DPPH[Krz+97], and the EDMR signal of a semiconductor device, simultaneously. In this case, the signal of the internal oscillator of one lock-in-amp is used as the reference signal of the second one. The advantage of this method is the in-situ calibration of the magnetic field inside the cavity during a measurement. A more detailed description of this technique is found in section 13.3.

A photo of the experimental setup is depicted in Figure 16. The main elements are marked with colored boxes and labels. Each plays an important role in the realization of EDMR experiments and influences the quality of spectra. One main goal of this study was to gain experience in performing EDMR experiments and to seek equipment and measuring techniques that provide optimal results. In the following sections each of the marked elements is described in more detail. The focus lies on the factors that influence the quality of measurements, as well as adaptions and replacements that were done to the original setup. In some sections a comparison of different devices is given in order to find an optimum, or to highlight advantages and disadvantages of certain solutions. This section gives guidance in understanding the most important aspects of setting up an EDMR experiment.

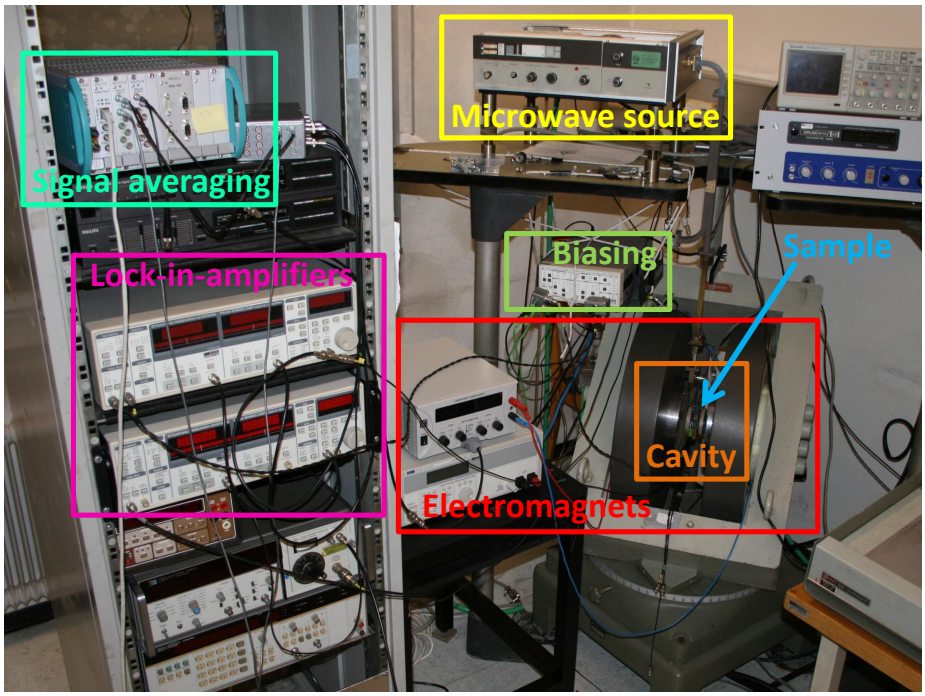

Fig. 16: Photo of the experimental setup with the most important elements marked.

7 Electromagnet

The most important part of an ESR or EDMR experiment is a stable, homogeneous, and well defined magnetic field. These properties influence the resolution, the accuracy of the measured g-value, the SNR, the signal averaging of multiple scans, and more. The required magnetic field of $B \approx 3000\,\mathrm{G}$ is generated by electromagnets where the sample is placed in the center of the gap between the pole shoes, where the magnetic field is the most homogeneous. Modern ESR spectrometers not only contain a very constant current source, but also a feedback loop for additional stability. A hall probe measures the magnetic field and with the help of this signal the current source can correct instabilities. The coils of the electromagnets are usually water-cooled, since there is a lot of power dissipated in the wires, which is heating the whole system.

7.1 Stability of the original setup

In this study a *Varian E9* spectrometer with a *Varian V-FR2503* power supply and the *Varian V3400* 9-inch electromagnets were used. For the first tests of ESR and EDMR experiments it was assumed that the stability of the current-source-feedback-loop system was working properly. However, when recording multiple scans it was observed that the zero-crossings of the lines were drifting over several G. This is displayed in Figure 17 where EDMR scans of a SiC-diode were recorded in a time range of about 10 h, as shown in the upper plot. Each individual scan took about 5 min. The average magnetic field of the zero-crossings was subtracted from the scans. The zero crossings are plotted in the lower plot. It is very clear, that the system is highly unstable and a total instability of $\Delta B \approx 10\,\mathrm{G}$ with a standard deviation of $\sigma_\mathrm{B} = 2.6\,\mathrm{G}$ is present.

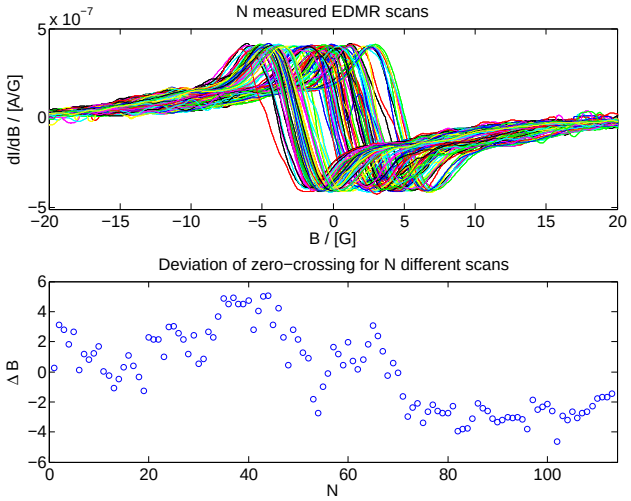

Fig. 17: 113 EDMR scans recorded with the original setup over a time period of $\approx 10\,\mathrm{h}$ (upper plot); zero crossings of the individual curves (lower plot).

What cannot be stated at this point is the time scale on which the instabilities occur. It can only be observed that fluctuations occur in the time scale of

individual measurements, which is, as mentioned, 5 min.

In order to get a better determination of the instabilities, the source was set on a constant magnetic field value of $B = 3300\,\mathrm{G}$ for a time of $t = 45\,\mathrm{min}$. Two measurements were performed, as follows.

First, the magnetic field was directly measured with a *Drusch RMN2* magnetometer. Here a magnetometer probe, containing a well known NMR standard, is put into the magnetic field and NMR transitions are induced by an RF-field with known frequency. From this, the magnetic field can be determined. The device performs this automatically and puts out a value every 450 ms, which can be recorded.

Second, the current through the coils, which is proportional to the magnetic field, was measured over the voltage drop across a water-cooled $20\,\mathrm{m\Omega}$ shunt resistor that was connected serially to the coils. The voltage measurement was performed with a *Keithley 196* digital multimeter.

Figure 18 shows both measurements. The upper plot contains the whole measurement, and the lower one is enlarged to a region where strong fluctuations occur. The magnetic field measurement is indicated blue, the current measurement is indicated red, and has been converted to the corresponding magnetic field in order to get a good comparison of both measurements. The mean magnetic field was subtracted. There is a good correlation between the two curves, which is important, in order to confirm the accuracy of the measurement. It is very clear from this plot, that the instabilities of the zero crossings are indeed caused by magnetic field instabilities. Especially from the lower plot it can be concluded, that the time scale of these fluctuations lies far below a scan time. Changes of up to 5 G are possible within a few seconds.

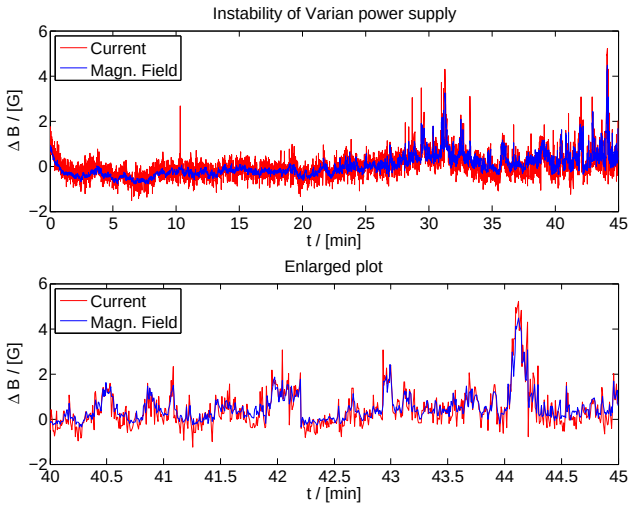

Fig. 18: Stability of a magnetic field of 3300 G generated by the Varian power source (upper) and enlarged plot (lower); The field was measured directly (blue) and through the current (red).

Is is obvious that this setup cannot be used for accurate characterization of samples, since the instabilities in the order of magnitude of the line widths occur

randomly and on small time scales. The shapes of the curves would be largely deviated and broadened. It is not clear, whether the instabilities are caused by the power source or by the feedback loop. For this reason it seemed reasonable to replace the power source with a more stable system, without a feedback loop. The first step was to find a suitable source that can provide higher stability of the magnetic field.

7.2 Stability of new current sources

In order to operate with more stable magnetic fields two different current sources were tested, powering the same set of coils as originally used. First a *TTi QPX1200* digital power supply and second an *HP 6269B* analog power supply were tested. The same experiment as in the past section was performed in order to get a quick test whether a source is suitable. Each source was used to generate a constant magnetic field of $B = 3300\,\mathrm{G}$ and the field was measured directly (blue) and through the current (red) over time, as shown in Figure 19.

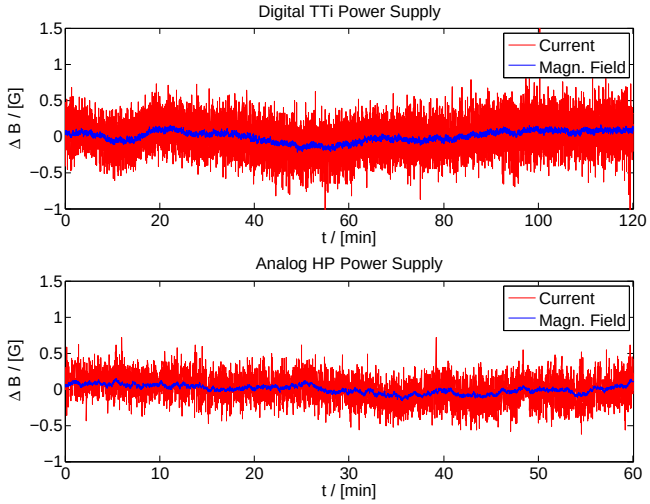

Fig. 19: Stability of a magnetic field of 3300 G generated by the *TTi QPX1200* (upper) and the *HP 6269B* (lower) power sources; The field was measured directly (blue) and through the current (red).

The instabilities of both sources are much smaller than of the original setup. The current measurement is more noisy than the magnetic field measurement due to bad shielding, which was not visible in Figure 18 because of the high amplitude of the instabilities. However, the important point is that both sources are a lot more stable than the original one. The results of the stability measurements are summarized in Table 1.

From this it can be concluded that improvements in stability of roughly a factor of 10 may be possible with both new sources. Considering that the long-term instability of the magnetic field, as seen in Figure 17, even a factor of 20 seems reasonable. For practical reasons, like shorter switching times and easier handling, the digital supply will be used to power the magnetic field, although

Table 1: Stability measurements of the three different power sources. The peak-to-peak instability ΔB and the standard deviation σ_B were calculated from the plots shown in Figures 18 and 19.

Source	ΔB/ [G]	σ_B/ [mG]
Varian	5.26	480
TTi	0.37	74
HP	0.30	58

the analog source is slightly more stable. A description of how the source is included in the setup and recent measurements that show the higher stability is given in the following section.

7.3 Improvements of the setup

The digital *TTi QPX1200* current source has good stability and can be used to produce the required magnetic fields. However, it cannot be used to sweep the magnetic field, as it is needed for ESR and EDMR experiment, because the steps of the source are not fine enough. For this reason, it is only used to generate a constant magnetic field of $3000 - 4000\,\mathrm{G}$. The scan is performed by a second set of coils, powered by an additional sweepable current source.

Adaptions of the electromagnet

The new system contains two separate coil systems, powered by two individual power sources. The whole setup is shown on the photo in Figure 20. On the one hand, there is the old set of coils, powered by the *TTi QPX1200* current source which is used to generate a field close to the resonance. On the other hand, there is a second set of coils (located behind the big coils, indicated by the yellow arrows), powered by an *EA-PS 3032-10B* current source that can scan the magnetic field over a range of up to 115 G (controlled by an analog input with a range of 0...10 V), starting from the point that is set on the other source. For safety, both power sources are protected by flyback diodes, connected in parallel to each coil.

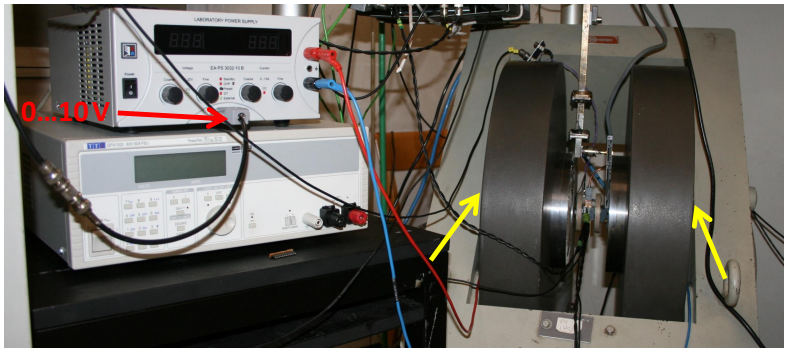

Fig. 20: The new magnet system contains two power sources and two sets of coils.

A disadvantage of this system is that the scan range is limited by the number of loops in the scan coils, and the maximum current of the *EA-PS 3032-10B* supply. Therefore, only a range of 115 G can be investigated during one scan. For this reason, a resonance peak cannot by found quickly, by scanning a larger range, and the peak can only be searched step by step. However, the performance and stability of this setup is orders of magnitude better than the original setup, as shown in the next section.

Stability of the new setup

The stability was first tested by looking at the magnetic field at a static point over a period of one hour, and observed with the *Drusch RMN2*. A comparison of the recording of the *TTi QPX1200* source only and the finished setup (*TTi QPX1200 + EA-PS 3032-10B* sources) is depicted in Figure 21. It can be concluded from the graph, that adding the second set of coils and the EA power source for scanning does not affect the stability.

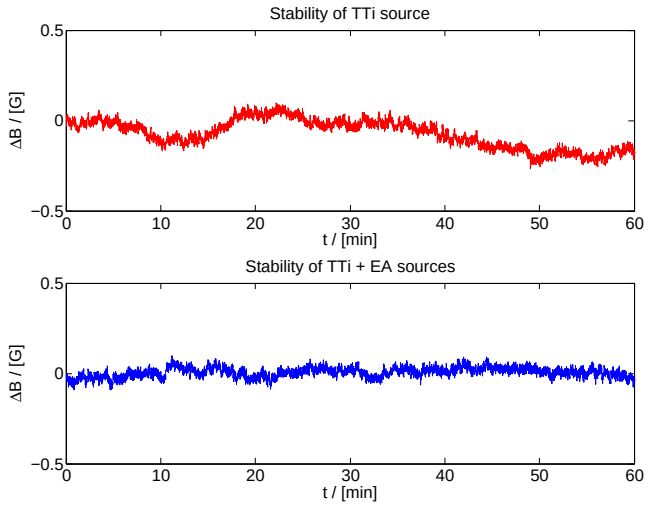

Fig. 21: Stability of a magnetic field of 3300 G, generated by the *TTi QPX1200* (upper) and the *TTi QPX1200* combined with the *EA-PS 3032-10B* (lower) power sources; The field was measured directly with the *Drusch RMN2* magnetometer.

A second very important test measures the stability and linearity of the slope of the magnetic field during a scan. Therefore, several scans were performed at different set static magnetic field strengths. The scans showed good linearity and a very constant slope. The slope was calculated by averaging five scans and the magnetic field B dependent on the control voltage of the sweep $V_{\text{sweep}} = 0...10\,\text{V}$ and the static field B_{static} is given by the equation

$$B = 11.55(1)\,\text{G/V} \cdot V_{\text{sweep}} + B_{\text{static}} \quad . \tag{57}$$

Finally, the stability during measurements was tested by performing the same EDMR scans of a SiC-diode, as described in section 7.1, and again, ob-

serving the positions of the zero-crossings. The 212 scans that were taken over a time of about 16 h are depicted in Figure 22.

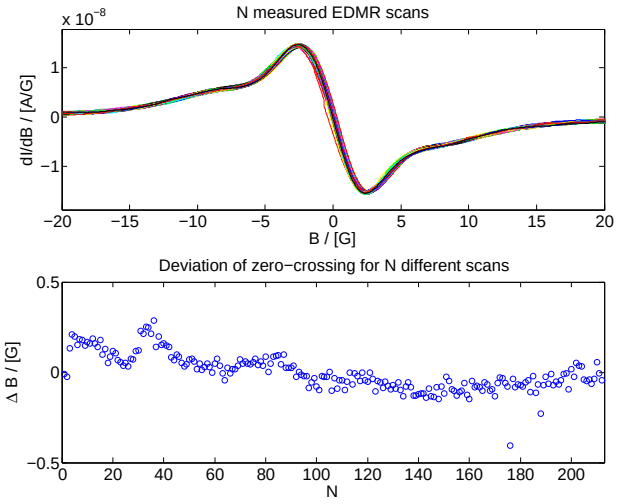

Fig. 22: 212 EDMR scans recorded with the new setup over a time period of ≈ 16 h (upper plot); zero crossings of the individual curves (lower plot).

As expected, the result is much better than with the old system. Big shifts of the lines did not occur any more. The spectra overlap very well, which is necessary for long term scans and good signal averaging. The standard deviation of the zero crossings is 0.1 G compared to 2.59 G determined from the scans shown in Figure 17.

It can be concluded that the exchange of the power source improved the whole experimental setup in order to perform good and reliable EDMR and ESR measurements. The stability of the magnetic field could be increased by a factor of about 25. This stability of the magnetic field, however, is not necessarily equal to the accuracy of the center line of a recorded scan. This would only be the case if the magnetic field was not monitored during scans. By including a calibration method into the measurement procedure the accuracy can still be increased. This method is discussed more closely in section 13.3.

8 Microwave source

A stable microwave source is as important as a good and stable magnetic field in order to perform ESR and EDMR measurements of high accuracy. The microwave source that was used in this study was the *Varian E-101* microwave bridge that generates microwaves of up to 200 mW power using a klystron. The advantage of this system is that it is self stabilized to the resonant frequency of the cavity. A disadvantage is the limitation in power and the requirement of additional instruments in order to determine the frequency. The following section gives a description of the microwave source and shows stability measurements that were performed.

8.1 Varian E-101 microwave bridge

The *Varian E-101* microwave bridge with a maximum output power of 200 mW was used as the source in this study. The microwaves are generated by a self stabled reflex klystron. The functionality of reflex klystrons is more closely described in section 4.1. In order to minimize reflections and to maximize the power injected into the cavity, a microwave source must generate microwaves of the resonant frequency of the sample cavity. This is the reason why the use of a reflex klystron is advantageous. During experiments, the system always sets itself on the resonance frequency of the sample cavity (through AFC). This can be very useful for long-term measurements, where the resonant frequency changes due to thermal expansion of the cavity, caused by temperature changes. This can be the result of heat, produced by the microwaves, or simply because of changes of the ambient temperature. Due to the self stabling mechanism, the system stays resonant and must not be monitored during measurements.

It is desired to gain information of the order of magnitude of the occurring instabilities, especially compared to the instabilities of the magnetic field. Therefore, stability tests were performed.

8.2 Stability tests

In order to test the frequency stability and investigate the effect of self heating, several cold starts were performed, while the frequency was observed with a frequency counter. As already indicated in Figure 15, 10% of the microwave power produced by the bridge was picked up by a directional coupler to determine the frequency using an *HP 5255A* frequency converter and an *HP 5335A* frequency counter.

The cavity was switched on, with the klystron locked to the cavity resonance frequency. The power generated by the klystron was 200 mW and the coupling into the cavity was optimized by observation of the reflected intensity. Before starting the measurement, the system was switched off in order to return to ambient temperature, since the cavity heats up during the process of optimizing the coupling. Then the microwave was turned on and the frequency was observed with the frequency counter.

Figure 23 shows the dependence of the frequency measured on three different days, with exponentially fitted curves (black) and the equilibrium temperature derived from the fit (dotted). The pink data points were measured for a quick test over a time period of 35 min. Since it can be seen from the fit, that the

equilibrium temperature was not yet attained, a second measurement over a time of 135 min was performed (red), and a third short one on the next day for 60 min (blue). After about 90 min the cavity reaches the equilibrium temperature and only small fluctuations remain. It is very clear, that the ambient temperature defines the equilibrium frequency. The change of equilibrium frequency between the measurements that were performed on different days is $\approx$ 500 kHz or, in other words, $\approx 5{\cdot}10^{-5}$ of the operating frequency and, thus, very small regarding the long time in between. As already mentioned, the equilibrium is reached after $\approx$ 90 min. What remains are very small fluctuations due to small ambient temperature changes and general instabilities of the microwave system. These instabilities have been determined as not being larger than 5 kHz which is $\approx 5 \cdot 10^{-7}$ of the operating frequency.

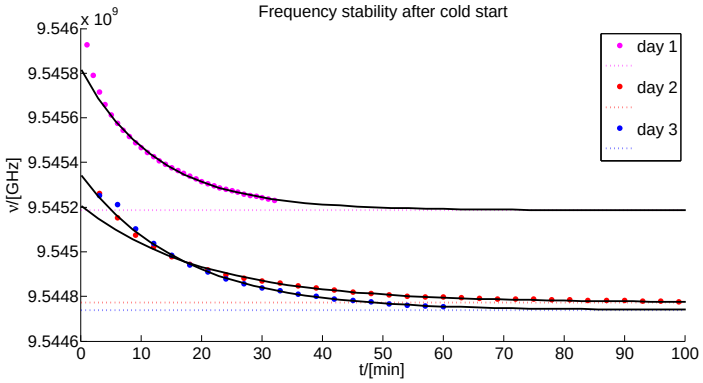

Fig. 23: Thermalization curves and exponential fits of the microwave measured after a cold start on three different days. The dotted lines indicate the equilibrium frequency after thermalization derived from the fits.

It can be concluded that the relative instabilities due to temperature changes, as well as instabilities of the source itself, are orders of magnitude smaller than those of the magnetic field determined in section 7. A thermalization time of about 90 min is sufficient in order to obtain stable conditions for individual EDMR scans of several minutes. It is not necessary to record the frequency more than once per scan.

9 Resonant cavities

Microwave cavities are essential for EDMR experiments in order to provide enough power to saturate the spin systems. The angular frequency times the energy that can be stored is the product of the input power and the Q factor. Therefore, it is beneficial to use a cavity with high Q. According to equation (54) a good conductor reduces the skin depth and, therefore, results in a higher Q. For this reason, commercially built cavities are often silver plated inside. There are many different geometries and different modes available. However, the cavities used in this study are all rectangular TE_{10m} cavities. The tested systems were a commercial cavity and two custom built ones. This section describes the different systems and give a comparison of their performance.

9.1 Varian E-232 TE_{104} dual cavity

The *Varian E-232* cavity system is part of the original *Varian E9* spectrometer accessories. A photo is shown in Figure 24. It is a silver plated cavity with a high Q and consists of two TE_{102} cavities put together. It allows for double measurements of a device and a reference standard as discussed in section 13.3. An advantage of this cavity is, that the modulation coils are included in the cavity sidewalls of each individual cavity and, therefore, two different modulation frequencies may be used.

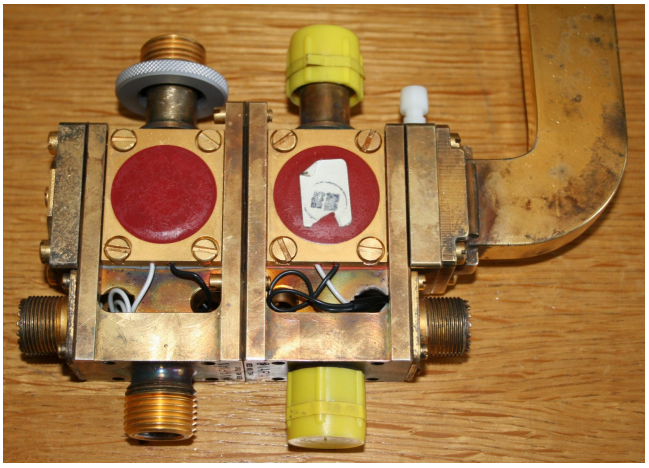

Fig. 24: Photo of the Varian E-232 TE_{104} cavity.

The coupling of the microwaves into the cavity can be adjusted with an iris that can be changed with a teflon screw, as depicted in Figure 25. Turning the screw changes the optical length to optimize the transmission of waves from the waveguide into the cavity. The coupling is first coarsely set by maximizing the size of the absorption dip in the power curve of a microwave source in scan mode, as it is indicated in Figure 11 c). Then it is optimized by minimizing the reflected power with the microwave source locked to the resonance frequency of the cavity.

Although this cavity has many features and a high Q, it was less used than the cavities described next. This is because the other cavities were built for

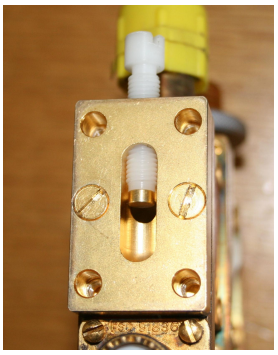

Fig. 25: Hole with iris to optimize coupling into the cavity.

testing purposes. One goal was to gain experience building cavities, and more attention was given to the custom built cavities. A second reason was that the sample holders were customized for the other cavities and are simply too short to fit into this system. However, this system is very sophisticated and also has accessories that allow for low temperature measurements; It should be considered for future experiments.

9.2 Custom built TE_{103} Cavity

The TE_{103} cavity was mainly used to demonstrate the benefit of double measurements, as described in section 13.3. It is shown in Figure 26. This cavity was built from a piece of waveguide, using equation (52) to determine the dimensions and sample hole positions. The coupling from the waveguide is obtained by a coaxial line that picks up the microwaves from the waveguide through an antenna. At the end of the line, which is put into the cavity, the outer conductor is connected to the inner one with a loop. The AC current flowing through the loop generates an alternating magnetic field that can propagate in the cavity. The coupling is optimized by adjusting the position of the loop in the cavity.

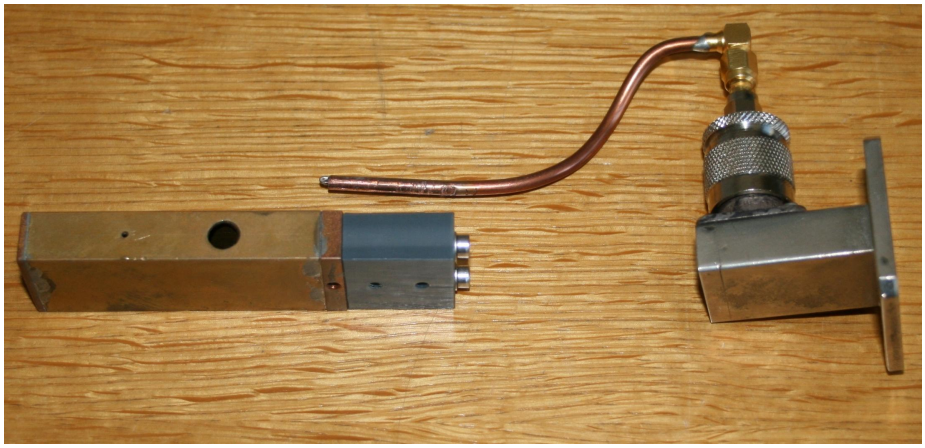

Fig. 26: Photo of the TE_{103} cavity.

9.3 Custom built TE_{102} Cavity

The TE_{102} cavity was built from a piece of waveguide with the goal of having a cavity with high Q in order to perform measurements with very high SNRs. According to equation (54) the TE_{102} mode offers the highest Q. A photo of the cavity is shown in Figure 27. For the microwave coupling into the cavity the same iris as for the TE_{104} (see Figure 25) can be used.

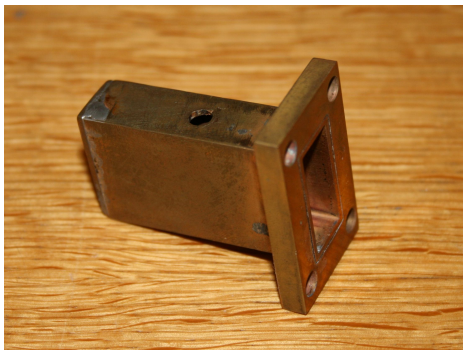

Fig. 27: Photo of the TE_{102} cavity.

As discussed in the next section, the Q of this cavity turned out to be smaller than the one of the other cavities. This may be caused by solder that has leaked into the corners during the fabrication.

9.4 Comparison

The different cavities were compared by performing the same measurements of a SiC diode with each cavity, revealing factors that may influence the performance of a cavity.

Q factors

First, the Q factors were determined for the different cavities. Every cavity was measured empty and loaded with a SiC diode on a sample holder, with two different orientations to the magnetic field. The measurements were performed at 200 mW microwave power. The coupling was optimized by minimizing the reflected power at the resonance frequency of the cavity. The klystron was then set into scan mode and the absorption peak of the microwaves reflected from the cavity were fitted with Lorentzians. The Q factors were determined from the widths of the Lorentzians. A comparison of the Q factors of the cavities is shown in Table 2. The loaded Q was determined for two orientations of the crystalline c-axis (c-axis) with respect to the B-axis.

The silver plated commercial *Varian E-232* TE_{104} cavity shows the highest Q of all systems, and for all three measurements. The custom built cavities have lower Q factors, but the difference is not as large when they are loaded. It was already mentioned that the TE_{102} cavity has a smaller Q than expected. Especially when compared to the TE_{103} that was built from the same piece of waveguide this is surprising. However, it is desired to build a new TE_{102}

Table 2: Q factors of the different cavities. Each cavity was measured unloaded (Q_0), with a sample with c-axis parallel ($Q_{||}$) and perpendicular ($Q_\perp$) to the magnetic field.

Cavity	Q_0	$Q_{||}$	$Q_\perp$
Varian TE_{104}	6700	3500	4400
Custom TE_{103}	4100	3100	3500
Custom TE_{102}	4200	2600	3000

cavity that is also silver plated in order to reach comparable Q factors as the commercial system.

It was observed during the experiments that sometimes slight changes in the position of a sample may have large effects on the width of the absorption peak and, therefore, on the Q. For this reason the values in Table 2 should only be interpreted as estimates.

Signal-to-noise ratio (SNR)

Next, the cavities were compared by recording scans of the SiC diodes and determining the SNR. Again, the samples were investigated at 200 mW power and in two different orientations. For every measurement eight scans were recorded and averaged, and the SNRs were determined from the height of the resulting spectrum divided by the standard deviation of the flat part of the curve. The results of the different measurements are shown in Table 3. All the values have been normalized to the highest occurring value.

Table 3: SNR of the different cavities. The sample was measured with c-axis parallel ($SNR_{||}$) and perpendicular ($SNR_\perp$) to the magnetic field.

Cavity	$SNR_{||}$	$SNR_\perp$
Varian TE_{104}	1.00	0.85
Custom TE_{103}	0.29	0.20
Custom TE_{102}	0.21	0.24

The *Varian E-232* cavity shows the best result again. However, the situation is very different when looking at the shape of the spectra. Figure 28 shows the spectra with the c-axis of the diode parallel to the magnetic field. The quality of a spectrum, besides the SNR, also lies in the resolution of the hyperfine peaks, occurring about 6 G left and right the center line. Here, the resolution of the spectrum recorded with the TE_{104} cavity is much worse. There are two plausible reasons to explain this.

First, it can be caused by unknown geometrical factors. As already mentioned above, sometimes small changes of the sample position can affect the coupling and the Q of a cavity. Since there is no mechanically stable sample holder available for this cavity, it may be the cause for the different line shape. Yet, this explanation is unlikely, since the Q and the SNR are very good.

Second, it is possible that the worse resolution is caused by power broadening. This cavity has the highest power present inside due to the highest Q.

This may result in power broadening, that is not yet present, when using the other cavities with the same input power.

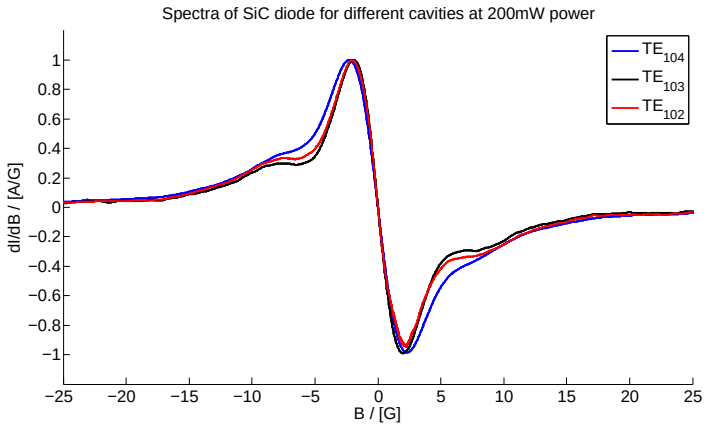

Fig. 28: EDMR spectra of a SiC diode recorded with different cavities using an input power of 200 mW.

In order to get a more clear picture about where the different line shape comes from some measurements at different input powers were performed.

9.5 Power dependence

The power dependence of the shape of a spectrum was investigated using the TE_{104} cavity, where the effect is expected to be the highest, due to the highest Q. The SiC diode was measured at different powers with the c-axis parallel to the magnetic field. Here the hyperfine splitting can be seen very clearly. Figure 29 shows the recorded spectra, normalized to the same size in order to get a better comparison of the line shape.

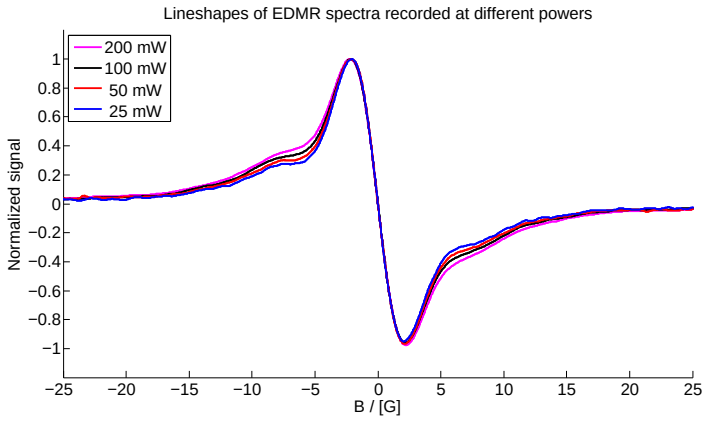

Fig. 29: EDMR spectra of a SiC diode recorded with the TE_{104} cavity at different microwave powers. The signals are scaled to the same size in order to get a better comparison of the line shape.

It can be observed that indeed the curves with higher power have less structure in the side peaks. However, the SNR increases with power as the total signal height increases which is shown in Table 4.

Table 4: The signal S_{EDMR} and the signal-to-noise ratio $SNR_{||}$ of a SiC diode measured with the Varian TE_{104} cavity at different input powers P_{MW}. The values are divided by the highest value of each column.

$P/\,[mW]$	S_{EDMR}	$SNR_{\|\|}$
200	1.00	1.00
100	0.48	0.85
50	0.28	0.32
25	0.17	0.23

The absolute signal height is increasing linearly with the power. The SNR has roughly a similar dependence. The conclusion that can be made from these measurements is that it must be considered carefully whether broadening effects occur at the operating power. A trade-off has to be made between a high SNR and a good resolution of structures in the spectrum.

If the structures to be resolved in a spectrum are narrow, broadening should be reduced to a minimum in order not to lose information. It may be favorable to attain good SNR by signal averaging instead of high powers, which results in longer measuring times.

Generally speaking, the choice of cavities can have a big influence on the results of the measurements. Unfortunately it is not always easy to compare measurements, since factors that are difficult to reproduce may play a role. These are mainly geometrical factors of the exact sample position and orientation in the cavity. Slight changes may deviate the field distribution in a way that the measurements differ a lot.

10 Sample holders and mountings

This section describes the sample holders that were used to put the sample in the cavity and to bias it. Therefore, electrical connections had to be integrated into the sample holder. PCBs offer a possibility of mechanically stable sample holders with electrically conducting paths. A plastic mounting system was built in order to hold both the cavity and the PCB holder in a stable position.

10.1 Printed circuit board sample holder

The PCB holders that were built are shown on the photo in Figure 30. The top PCB is a simple holder, used for first tests. It was produced manually with copper layered PCBs. Due to the simple production equipment it only has four traces of a diameter of about 0.5 mm, which limits the variety of devices that can be investigated. Of course, diodes or MOS field effect transistors (MOSFETs) can be operated with four traces, but certain test structures often require a larger number. For this purpose, a new holder was built, which is shown on the bottom. It is a professionally built PCB with gold traces. It has twelve parallel traces and, therefore, offers many possibilities regarding the connection of the devices. Also, the multiple connection of the device electrodes in order to reduce noise, as described in section 11.3, is possible with this holder. In order to keep influences on the Q factor of the cavity small, the PCBs and the gold traces are built as small as possible. The part that is outside the cavity is covered with a second gold layer that is grounded for additional shielding.

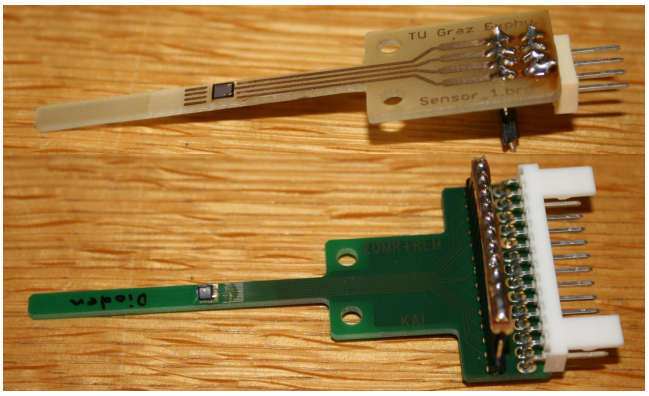

Fig. 30: Photo of the first PCB sample holder (top) and the upgraded version (bottom).

The semiconductor devices that were investigated were soldered onto the PCBs. The contact pads on top were bonded with gold wires, just as in conventional chip manufacturing. The traces on the PCBs make the connection to pins where a cable can be plugged in. In order to protect the devices from electrostatic discharge (ESD), a jumper shorts all traces and is only removed when the device is installed in the cavity and connected to the measuring units. For protection against mechanical damage, the device itself can be covered under a drop of synthetic resin. The PCBs are all reusable. A device can easily be removed and a new one attached and bonded.

10.2 Mounting of the cavities and PCBs

A plastic mounting was built in order to obtain a mechanically stable setup of the cavity and the PCB sample holder between the magnet poles. The advantage of plastic is that it does not affect the magnetic field. A photo of the mounting system is shown in Figure 31.

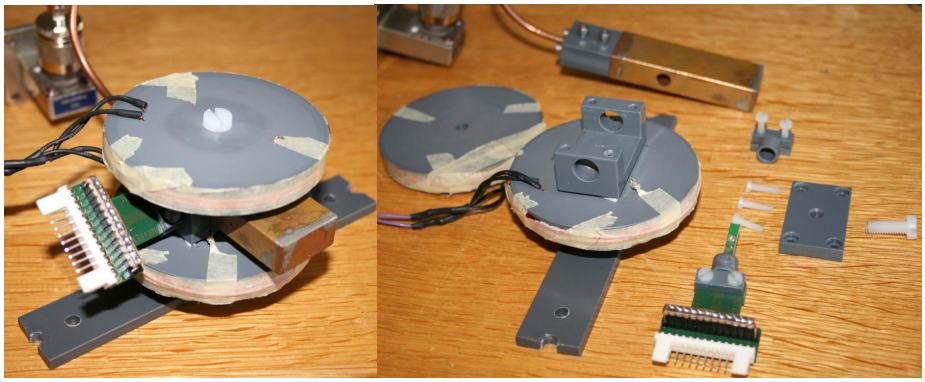

Fig. 31: Photo of the mounting for the cavities and PCBs, assembled (left) and disassembled (right).

The whole mounting can be screwed onto one of the magnet poles with the plastic ground plate. The cavity is held by a plastic plate with teflon screws in the center of the mounting, so that also the hole for the sample is in the center. The PCB with the sample is screwed to plastic cylinders that can be inserted into the holes of the mountings. The modulation coils for the lock-in-amplification are screwed to the mounting so that the sample position is in the middle of the coils, where the modulation field is the most homogeneous.

This system offers the possibility of rotating the sample in the magnetic field. This is important to gain information of the spherical symmetry of the g-tensor of the sample. The rotation axis is perpendicular to the magnetic field. In order to scan a device in all directions, three samples are required that are each attached to the PCB with a different orientation of the c-axis compared to the PCB axis (see Figure 32).

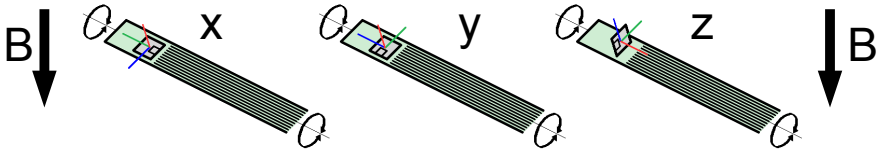

Fig. 32: Directions measurable with a rotating PCB holder. Three differently attached samples are required to determine the symmetry of the g-tensor.

11 Lock-in-amplification

Lock-in-amplification is essential for ESR and EDMR experiments. A functioning system contains two main components. First the amplifier itself, second the coils that modulate the magnetic field. Both systems used in this study are described briefly in this section, followed by further discussions of other influences and effects that should be considered.

11.1 Stanford Research SR830

The lock-in-amps that were used in this study are two *Stanford Research SR 830*. They have an internal oscillator with a wide range of frequencies. They can produce an output signal of up to 5 V amplitude which can be used for the modulation. The signal is also the reference signal for the phase detector of the amp. When using both amps for double measurements (see section 13.3) the oscillator of one amp is used for the modulation and as reference for the second amp. The *Stanford Research SR 830* also contains several noise filters, such as a line frequency and double line frequency filter, which were both generally activated for measurements. The output of the phase detector has two channels and can either display the cartesian coordinates X and Y, or the polar coordinates r and ϕ of a measured signal. Usually X and Y were recorded and used to calculate r afterwards. This was due to phase jumps of ϕ, often occurring in the middle of a scans.

11.2 Modulation coils

The modulations coils that were used for most experiments are a custom built set of Helmholtz-coils which are shown in Figure 33. These coils can be used for the TE_{103} and TE_{102} cavities while the TE_{104} cavity has modulation coils built into the sidewalls. The coils were built in order to obtain 1 G modulation when using the 5 V output of the *Stanford Research SR 830*. For higher modulation amplitudes, a *Phillips FR 153* audio amplifier can be used. The coils have a diameter of 3.5 cm and 80 turns each, which results in a low impedance. This is important in order to modulate at high frequencies. In the range below 10 kHz the coils have almost negligible impedance, compared to the ohmic resistance of the modulation circuit.

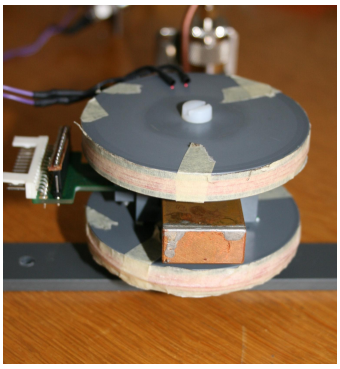

Fig. 33: Photo of the modulation coils.

11.3 Induction

Induction is a problem that occurs when using a large set of modulation coils. In the simplest case, a diode is connected with two traces. This is indicated by the red lines, in the top image of Figure 34. If there is a flux Φ from the modulation field through the area A between the lines, it will induce a signal additional to the diode current, which is indicated in the bottom image. The induced current I_{ind} is given by the law of induction

$$U_{\text{ind}} = R_{\text{l}} I_{\text{ind}} = -\frac{\mathrm{d}}{\mathrm{d}t}\Phi = -\frac{\mathrm{d}}{\mathrm{d}t}\int_A \mathbf{B}\cdot d\mathbf{A} \quad . \tag{58}$$

This induced signal is has the same frequency as the EDMR current and will also be amplified by the lock-in-amp. It will appear as a constant offset added to the spectrum. For high modulation frequencies and, therefore, a large time derivative, it can be orders of magnitude higher than the EDMR current. Additionally, all noise and fluctuations of this constant signal will also appear in the spectrum. Minimizing this effect is always desired. The induced current can be reduced by lowering the flux through the lines. This can be attained, on the one hand, by reducing the spacing between the traces and, on the other hand, by using smaller modulation coils. A different possibility is to use three traces to power the diode. The green line in Figure 34 is connected such that the current going to the device is divided in two equal parts. The current that comes from the device goes back through one trace in the middle, as indicated in the top image. Therefore, two loops around equal areas are formed. If now the changing flux from the modulation field induces current in the loops they will cancel out, as indicated in the bottom picture.

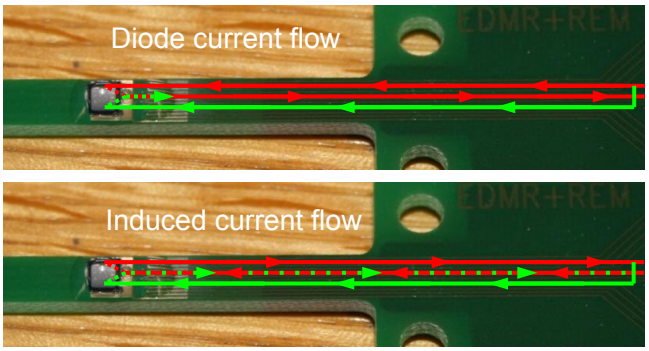

Fig. 34: Diode current and induced current flow.

With this method, the offset induced by the modulation field itself can be reduced which, in some cases, allows for higher sensitivity of measurements. A disadvantage of the method is that it only works if the loops go around equal areas. This is often not easy to realize, because the shape of the bonding wires that connect the traces with the metal pads of a chip cannot be controlled so well. They may have different bends resulting in the areas of the two loops being different; In this case the method does not work so well.

12 Biasing and pre-amplification

SDR experiments require both biasing of the device and a measurement of the current. The current is generally very small and needs to be amplified. This is performed by a lock-in-amplifier. However, for shielding and noise reduction purposes, it is desired to have the electronic measuring units, such as the lock-in-amp, not too close to the electromagnets. The biasing unit should, however, be as close as possible. In this study the *Stanford Research SR570* current amplifier was used to bias the devices. The big advantage of this device is that it contains a current-to-voltage converter that pre-amplifies the signal before it is transferred to the lock-in-amp. This way noise can be reduced to a minimum.

The amplifier has two Bayonet Neill Concelman (BNC) connectors. The first is the input of the current to be measured. There can be a bias voltage applied between the pin and the guard of the connector using a computer software and an RS-232 interface. The second one is a voltage output proportional to the input current. A disadvantage of the BNC connectors here is that both the pin, as well as the guard, are used to transfer signals. Therefore, there is no grounded shield if just a coaxial cable is connected. In order to obtain shielding of both lines, metal boxes were built that connect both lines to the inner lines of separate coaxial cables. Both guards of the cables and the metal boxes are grounded, the lines of the current amplifier are potential free. Figure 35 shows the front panel of the *Stanford Research SR570* and the metal boxes plugged to the BNC connectors.

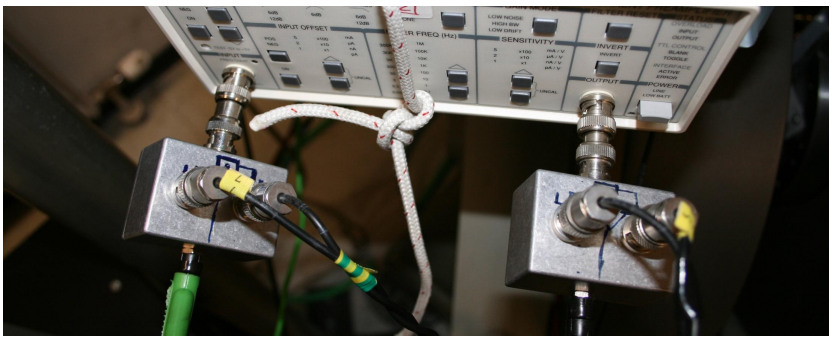

Fig. 35: Photo of the pre-amplifier and the shielding boxes.

Another advantage of using this model are the different filters in the device. By using filters, the noise can be reduced, before the lock-in-amp does the main filtering and amplifying. Also, when using more sophisticated techniques like (spin dependent) charge pumping, a filter is required. Therefore, the *Stanford Research SR570* is a very suitable device for EDMR experiments.

The SiC diodes that were measured in SDR experiments for this study were forward biased at 2.37 V. At this voltage, the recombination current has a maximum and the highest SDR response is expected [Aic+12]. Generally, when performing SDR experiments, it is useful to record the current-voltage (IV)-characteristics of the device first and look for the voltage where the slope results in a ideality factor of $\eta \approx 2$. The region where η is closest to 2 is where recombination is the dominant transport mechanism.

13 Signal averaging

So far, only factors that influence the generation of ESR and EDMR response have been treated. However, not only the generation of signals, but also the data capture and signal averaging play an important role in the quality of spectra. The SNR can be reduced by averaging many individual scans. This section gives a general description of how data capture and signal averaging have been performed in this study. An idea of automatically calibrating the magnetic field by measuring the EDMR sample and simultaneously an ESR standard is also explained.

13.1 Data capture

For the data capture a programmable *Jäger ADwin Pro II* eight channel ADC-DAC was used. The advantage of this device is that it can be used both to sweep the current source of the magnets and record the signal from the lock-in-amp. The device has 16 bit resolution and short switching times. It allows for recording of one measurement point of the spectrum many times, before going to the next step of the sweep. This gives an opportunity of including some signal averaging already in the recording. For every point of a spectrum the response of the lock-in-amp is recorded 10000 times within 20 ms, in order to reduce noise influenced by line cables. This averaging is performed automatically by the software of the device and puts out the mean value and the standard deviation for each point of the spectrum.

The recording and plotting of the standard deviation reveals a second benefit of this procedure in addition to signal averaging. The standard deviation will be large at points of a spectrum where the slope is steep. This is due to the fact that magnetic field changes result in a higher variation of the signal than when the slope is low. Therefore, the standard deviation plot can be used in order to optimize the measuring parameters by finding a minimum. With this method the scan speed and the waiting time for the magnetic field to stabilize for each point before recording the response can be set.

Figure 36 shows how the resulting response of a SiC diode for two different parameter sets is recorded by the *Jäger ADwin Pro II*. The curves on the left are the recorded spectra, which are the first derivatives of the actual spectra. The curves on the right are the standard deviation plots.

Both, a fast and a slow scan were recorded with a microwave frequency of 9.46 GHz. The blue line is a fast scan containing 1000 measurement points recorded with a lock-in time constant of 300 ms. There is no delay time between stepping to the next point of a spectrum and averaging the signal over 20 ms. The red line is a slow scan with 2500 steps, a time constant of 1 s and a delay of 100 ms.

The spectra look very similar but the standard deviation of the fast scan is much higher. This is due to the fact that the magnetic field is changing while the *Jäger ADwin Pro II* is already measuring and averaging the values. By minimizing the amplitude of the standard deviation plots, the scan speed and delay time can be optimized. However, the measurement time is desired to be low enough to perform multiple scans. The standard deviation plot is helpful but mainly in order to find a good parameter set for a certain desired scan time.

The standard deviation gives a measure of the slope at a certain point of

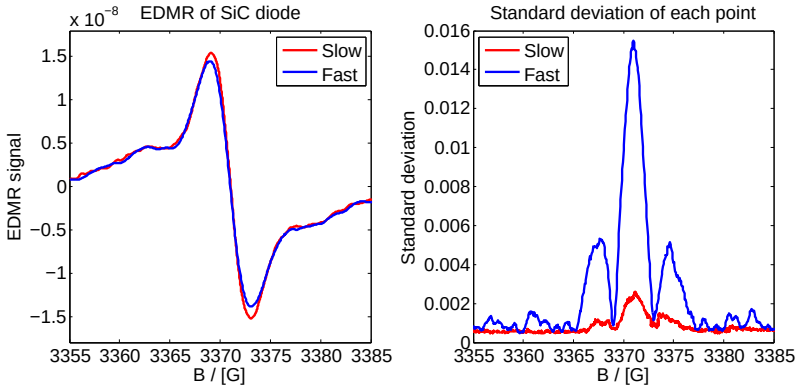

Fig. 36: EDMR response (left) of a SiC diode and the standard deviation for each measurement point (right) recorded by the *Jäger ADwin Pro II* for a fast scan (blue) and a slow scan (red).

the spectrum. For this reason, it can be beneficial to perform a scan with parameters that cause a high standard deviation, in order to gain information on how many changes in the slope there are in a spectrum. This test can be helpful in determining how many peaks a spectrum contains. For good results of a spectrum, a minimum should be approached. Further improvement of the SNR of spectra can be achieved by signal averaging.

13.2 Signal averaging

The main signal averaging is performed by forming the average of many individual scans. This is performed by computer software. First, every recorded scan is loaded and the magnetic field axis is determined from equation (57). Then the averaging of the curves is performed. This is obtained by a binning procedure. All measured points of all curves are put in one array. Then the magnetic field axis is divided into equidistant "bins", usually as many as there are measurement points in a single scan. The measurement points in each bin are averaged and the mean value is plotted versus the bin position. The result is the average spectrum of the input spectra. However, there are two procedures how the averaging can be performed depending on the goal:

Signal averaging for accurate g-value

To get an accurate g-value the spectra are averaged as measured. The zero crossing of the average spectrum can be used to determine the g-value. The accuracy of this value can be tested by obtaining the g-values of the individual scans and forming the average. The difference between the two determined values should be small. However, due to instabilities of the magnetic field, the differences between individual scans may be large. This would result in the average spectrum being broadened or the individual g-values having a large distribution. By accurately determining the magnetic field for every individual scan, this effect can be minimized, as explained in section 13.3.

Signal averaging for accurate line shape

To get an accurate line shape, the scans are shifted towards their zero-crossing before averaging them. This alignment to the center line helps minimizing effects caused by instabilities of the magnetic field during a scan. The average of the shifted curves has the most accuracy with respect to the line shape of a spectrum. A disadvantage of this procedure is that it can only be performed for samples where the signal is high enough to get a good reference point for the alignment.

The final spectra are obtained by shifting the spectrum averaged with the second procedure, to the center magnetic field, corresponding to the g-value obtained by the first procedure. As mentioned above, signals with weak response and unstable magnetic field may have a bad influence on both the obtained line shape as well as the accuracy of the g-value. The next section focuses on a method that helps to improve the results.

13.3 Double measurement with in-situ calibration

When performing signal averaging, as described above, the result is strongly dependent on the accuracy of the magnetic field axis of each individual spectrum. As shown in Figure 22 of section 7.3, there are slight deviations of the magnetic field, occurring due to instabilities of the setup. These instabilities occur on a time scale that is at least the duration of several measurements. They may be the result of ambient temperature changes. However, it can be assumed that the magnetic field is not the same for every scan. If the magnetic field was assumed constant, the resulting curves would have a larger distribution of their zero-crossings than if the magnetic field was determined for each curve separately. A common method to determine the magnetic field is to use an ESR standard such as DPPH [Krz+97]. However, it is often only used to determine the magnetic field once before and once after recording ESR/EDMR scans. A method where the calibration of the magnetic field is performed for every individual scan automatically is described next.

For this, a microwave cavity that offers positions for two samples is required. The TE_{103} cavity described in section 9.2 was used in this study. Additional to the EDMR sample, a weak DPPH sample was put in the cavity as calibration sample. Weak, in this case, means that the number of unpaired electrons in the calibration sample was determined to be smaller than 10^{15}. The recording of spectra with this calibration method requires a second lock-in-amplifier. The first one is used to measure the EDMR response through the current while the second one measures the ESR in the absorption. Two spectra are obtained, one containing the information of the EDMR sample and the other one containing the DPPH spectrum, with the very well known g-value of 2.0036. The influence of the samples on eachother is negligible.

On the one hand, the number of defects in EDMR samples is many orders of magnitude smaller than the 10^{15} unpaired spins of the DPPH sample. Therefore, the power absorbed by the EDMR sample has negligible effects on the ESR response of the calibration sample. Also, the influence of the ESR on the EDMR is very small. Since the EDMR signal is measured through the current, the ESR sample does not have any influence on the signal. Only the higher absorption of

power at resonance can influence the EDMR spectrum, since there will be less power in the cavity. Also this effect is negligible due to the very little power that can be absorbed by the weak calibration sample, compared to the large power stored in the cavity.

Figure 37 shows a scan where both signals were recorded; the ESR is shown in the top Figure and the EDMR in the bottom Figure. The zero crossing of the ESR spectrum is used to calibrate the magnetic field axis of both plots. This is performed using the known magnetic field at the zero crossing of the DPPH sample and the known slope of the scan (see section 7.3). This method gives a very accurate calibration of the magnetic field.

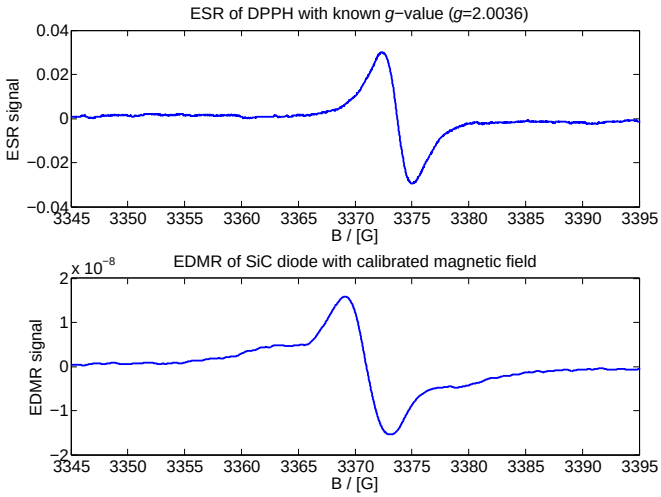

Fig. 37: Double measurement: ESR of DPPH (top) and EDMR of SiC diode (bottom). The magnetic field axis of both spectra was calibrated with the zero-crossing of the DPPH spectrum.

There are several benefits. The procedure can be included into the automatic measuring routine. The ESR is always recorded simultaneously to the EDMR and the analysis program can automatically calibrate the spectra with the zero crossing of the DPPH. This means that the magnetic field must not be measured or observed, and long term measurement instabilities are automatically corrected. This can be seen in Figure 38, showing the data from Figure 22. However, the calibration of the magnetic field decreases the standard deviation of the zero crossings from 0.1 G to 0.04 G. This means the accuracy of the determined g-values will also be higher using this method. Another benefit is the possibility of better alignment of samples with low and noise contaminated signals. The in-situ calibration is the only possibility to align spectra that do not show any clear reference point for an alignment.

13.4 Integration

The spectra that are measured are the first derivatives of the actual EDMR spectra, therefore, they must be integrated. This is performed automatically by

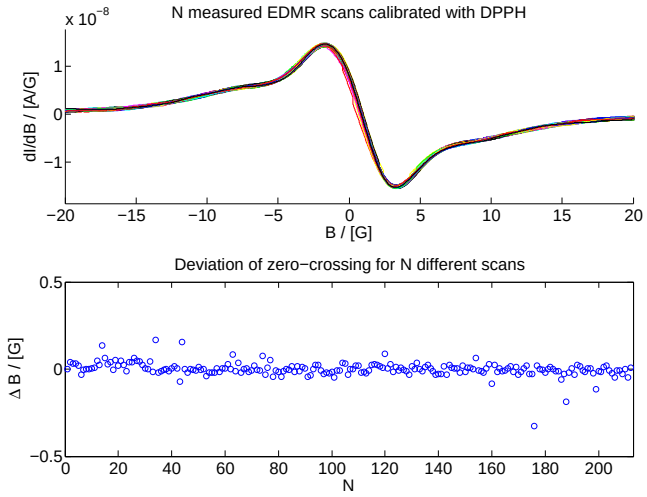

Fig. 38: 212 EDMR scans recorded over a time period of $\approx 16\,\mathrm{h}$ and calibrated with simultaneously recorded DPPH marker (upper plot); zero crossings of the individual curves (lower plot).

the software routine using the trapezoid method. Figure 39 shows the resulting spectrum of 16 lines from Figure 38 that have been averaged and integrated.

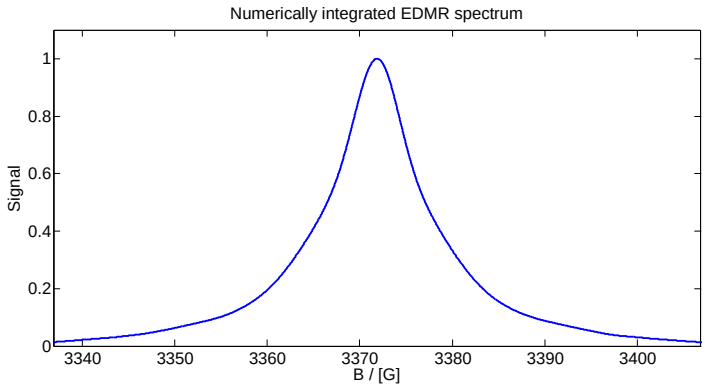

Fig. 39: Integrated spectrum of a SiC diode. 16 scans were averaged and numerically integrated.

14 Summary

An EDMR setup was developed that is capable of measurements with good stability and high resolution. The system was built around a *Varian E9* ESR spectrometer. The power source of the electromagnets was exchanged by a newer system with higher stability. Three microwave cavities were tested that can all be used to perform EDMR measurements. A system of sample holders and mountings was built that allows for mechanically table measurements and rotation of the sample in the magnetic field, in order to measure different crystal orientations. An operating program was written that can perform scans entirely automatically, without any monitoring. The data packages produced can be further processed with the developed analyzing software. This software automatically calibrates and averages the recorded spectra. The averaging is performed in two different ways, and both results are combined in the final spectrum. First, the average of the measured and calibrated curves is calculated, allowing for a very precise g determination. Second, the spectra are all shifted to their zero-crossings and, again, the average is calculated. This average has more precision in the line shape. Finally, the second spectrum can be shifted to the center magnetic field, determined from the first average. The resulting spectrum is then integrated.

The accuracy of the g can be increased by a method that measures the ESR response of a calibration sample, simultaneously to the EDMR recordings. With this method, slow changes in the magnetic field can be corrected up to a certain level. In the last section of this thesis the capabilities of the developed setup are demonstrated by showing recorded spectra and comparing them to spectra from a recent study.

Chapter III

Results

This final chapter focuses on measurements that were performed in order to demonstrate the capabilities of the setup. Therefore, a SiC diode was investigated and compared to reference measurements from a recent study [Aic+12]. The main results of this chapter were presented at the *European Conference of Silicon Carbide and Related Materials* 2012 in St. Petersburg [Gru+12].

15 Device characteristics

In order to perform EDMR experiments of a diode with good SNR, it is desired to use a bias voltage where trap-assisted recombination is the dominant transport mechanism. This is the case, when the ideality factor η from equation (16) equals 2. The forward IV-characteristic of the SiC diode was recorded in order to find a suitable biasing voltage. Figure 40 shows a semi-logarithmic plot of the characteristics (blue).

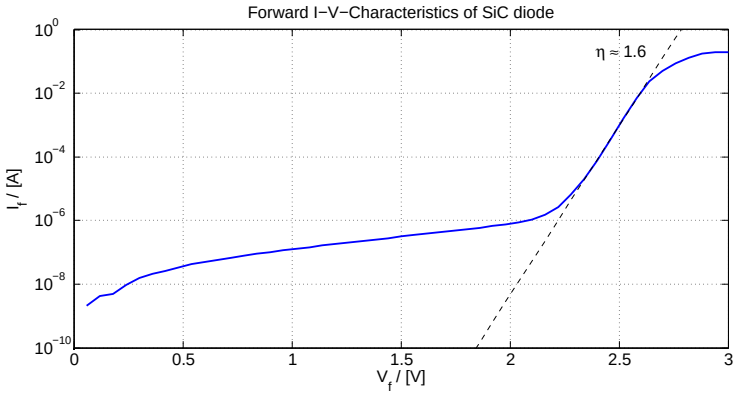

Fig. 40: Forward IV-characteristics of a SiC diode (blue) and fit of the recombination region (black).

The black dashed line is a fit of the region where the slope is the steepest and $\eta \approx 2$. In the regions that are flatter η is much greater and recombination is not the dominant transport mechanism. Therefore, the biasing voltage V for the following experiments is $V = 2.37\,\mathrm{V}$, which lies in the center of the recombination region.

16 EDMR measurements

Several EDMR measurements were performed in order to demonstrate the functionality of the setup. The data was compared to available results from a recent study that measured the same SiC diode [Aic+12]. The measurements were performed with the TE_{103} cavity (see section 9.2) and the in-situ calibration method with DPPH was applied (see section 13.3). The device was forward biased at 2.37 V using the *Stanford Research SR570*. The double-loop method, as described in section 11.3, was applied. Both, the ESR and the EDMR were recorded, using *Stanford Research SR 830* lock-in-amplifiers. The modulation was performed with the low-impedance Helmholtz-coils described in section

11.2. The modulation frequency was $\nu_{\mathrm{mod}} \approx 1\,\mathrm{kHz}$ and the modulation amplitude $B_{\mathrm{mod}} = 1\,\mathrm{G}$. 3000 data points in a range of 60 G were recorded with a lock-in time constant of $\tau_{LP} = 1\,\mathrm{s}$. The microwave power was 200 mW. Two orientations of the c-axis of the device with respect to the B-field were measured and compared to the reference.

16.1 EDMR with c-axis parallel to B

The resonant frequency for this configuration was $\nu_0 = 9.4609\,\mathrm{GHz}$. 16 traces were recorded and averaged, using the procedure described in section 13.2. The resulting curve is shown in Figure 41 as a solid line. The reference measurement is plotted as a dashed line. The bottom plot shows an enlarged view of a sidepeak for better comparison. Both measurements were performed with comparable equipment and parameters. They have been normalized and shifted to their center line.

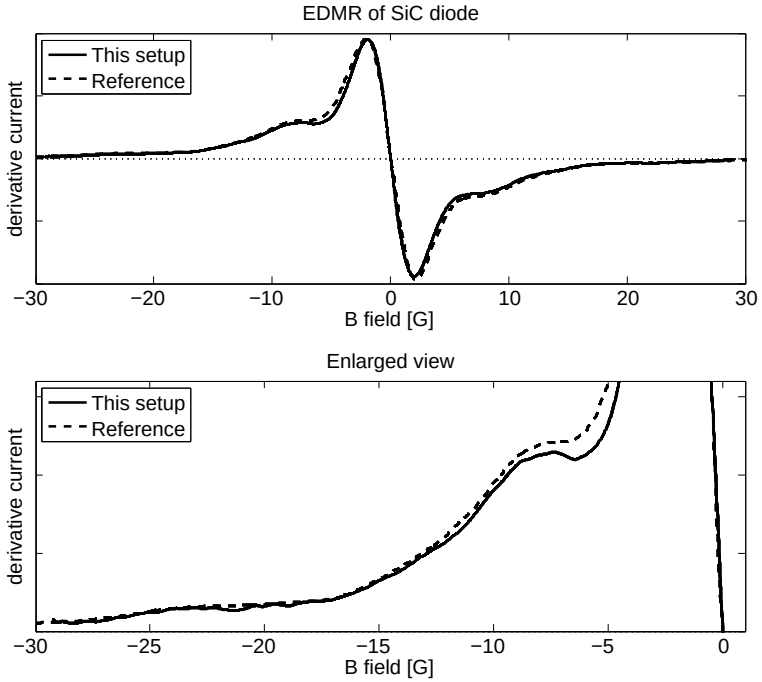

Fig. 41: EDMR of the SiC diode with c-axis parallel to B recorded with the described setup (solid) and the reference (dashed)[Aic+12]. The lower plot shows an enlarged view for better comparison.

The comparison reveals a very similar lineshape of the two curves. The reference curve has slightly better SNR while the measured curve has better resolution of the side peaks. Generally, the curves are in very good agreement. The g-factors determined from the curves are $g_{||} = 2.0052\,(3)$ (this setup) and $g_{||} = 2.0048$ (reference) [Aic+12]. These values are, therefore, in good agreement.

Both spectra have a very similar shape with a strong, narrow center line and

two strong sidepeaks 7 G left and right of the center line. Also a second, weak pair of sidepeaks can be found about 22 G from the center line in both spectra.

16.2 EDMR with c-axis perpendicular to B

The resonant frequency was $\nu_0 = 9.4569\,\text{GHz}$. The recorded spectrum is shown in Figure 42. For this configuration no reference spectrum is available for comparison. However, the spectrum again reveals some hyperfine structure, indicating good resolution of the setup. The hyperfine structure is less dominant in this orientation due to some anisotropy of the defect.

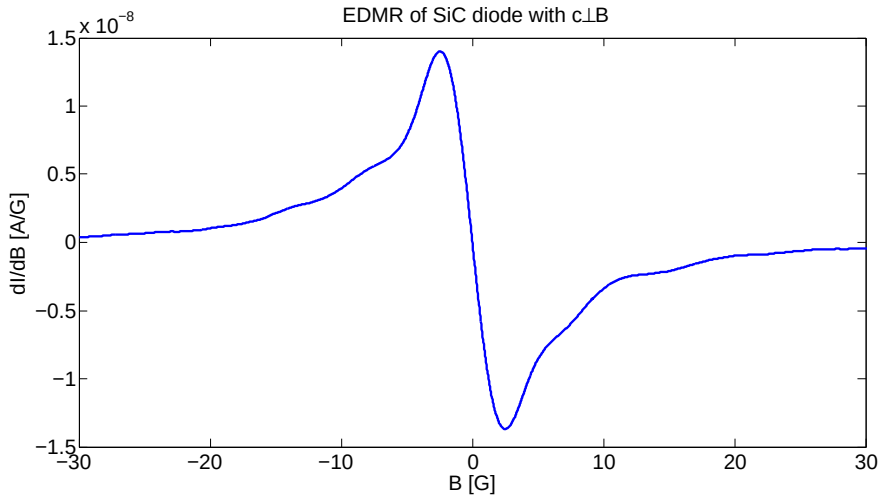

Fig. 42: EDMR of the SiC diode with c-axis perpendicular to B recorded with the described setup.

The g-value was determined as $g_\perp = 2.0003(3)$, compared to $g_\perp = 2.0005$ from the reference [Aic+12]. Again, the developed setup is in agreement with the reference.

Also this spectrum shows a strong center line and two pairs of side peaks at about 8 G and 12 G left and right of the center line. The different intensities and hyperfine constants are due to anisotropies of the hyperfine structure of the defect.

16.3 Integrated spectra

The recorded spectra, shown in Figures 41 and 42, were integrated numerically, as described in section 13.4. Both integrated spectra are shown in Figure 43. The upper graph contains the integrated spectrum of the SiC diode with the c-axis parallel to the B-field. The hyperfine peaks that could already be seen very clearly in Figure 41 are also easy to recognize in this graph. This indicates very high resolution of the peaks. The lower graph shows the integrated spectrum with the c-axis perpendicular to B. The small hyperfine peaks from Figure 42 are barely noticeable in the integrated plot. It can generally be stated that the upper spectrum is narrower.

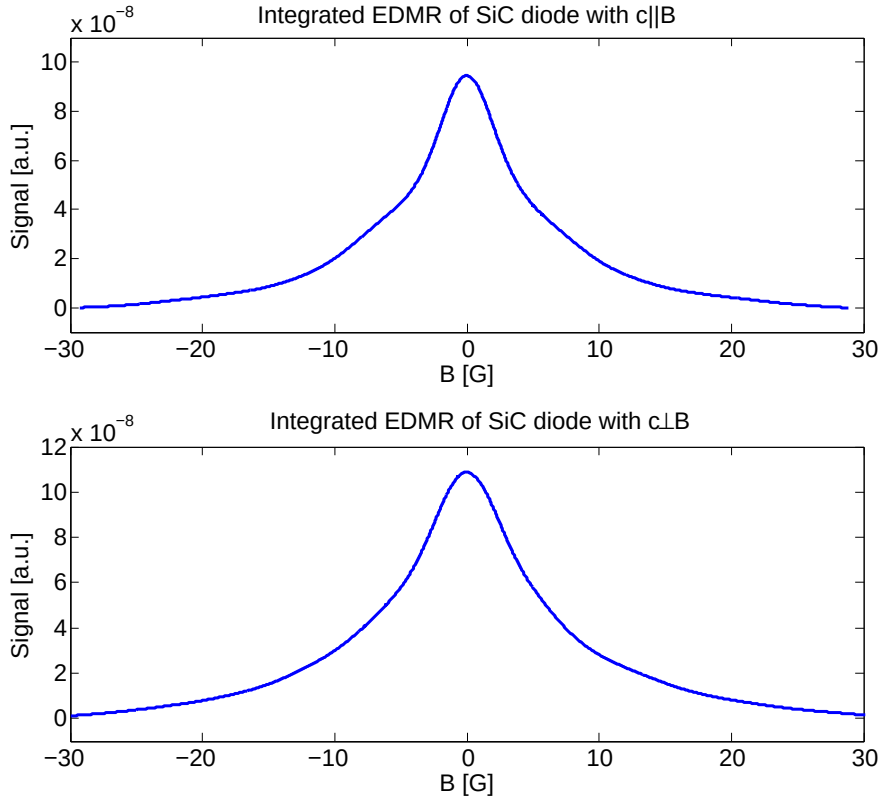

Fig. 43: Integrated EDMR spectra of the SiC diode with the c-axis perpendicular (top) and parallel (bottom) to the B-axis.

17 Summary

The spectra of the SiC recorded with the developed EDMR setup demonstrate its capabilities and reproduce the data from the cited study. Both, the shapes of the spectra, as well as the g-factors are in agreement. The measured g-factors are

$$g_{||} = 2.0052\,(3)$$

with the c-axis parallel to B, and

$$g_{\perp} = 2.0003(3)$$

with the c-axis perpendicular to B. Although the SNR was not as good as in the reference, the hyperfine peaks could be resolved better. This could be due the setup but also due to different stress applied to the, otherwise identical, SiC diodes. However, it can be concluded that the developed setup qualifies for further EDMR studies of new devices.lthough the SNR was not as good as in the reference, the hyperfine peaks could be resolved better. This could be due the setup but also due to different stress applied to the, otherwise identical, SiC diodes. However, it can be concluded that the developed setup qualifies for further EDMR studies of new devices.

Bibliography

[Aic+12] T. Aichinger et al. "A nitrogen-related deep level defect in ion implanted 4H-SiC pn junctions - A spin dependent recombination study." In: *Applied Physics Letters* 100 (2012).

[Aic07] T. Aichinger. "Implementation of the charge pumping method for MOS characterization into existing soft- and hardware environment." MA thesis. Karl Franzens Universität Graz, 2007.

[Aic11] T. Aichinger. Private communication. 2011.

[BHP46] F. Bloch, W.W. Hansen, and Martin Packard. "Nuclear induction." In: *Physical Review* 69 (1946), p. 127.

[FPS09] D.M. Fleetwood, S.T. Pantelides, and R.D. Schrimpf, eds. *Defects in Microelectric Materials and Devices*. CRC Press, 2009.

[Göb11] Holger Göbel. *Einführung in die Halbleiter-Schaltungstechnik*. Springer-Lehrbuch, 2011, p. 56.

[Got07] G. Gottstein. *Physikalische Grundlagen der Materialkunde*. Springer, 2007, 65ff.

[Gro67] A.S. Grove. *Physics and Technology of Semiconductor Devices*. John Wiley & Sons, 1967.

[Gru+12] G. Gruber et al. "An Extended EDMR Setup for SiC defect characterization." In: *Silicon Carbide and Related Materials 2012, Proceedings of the ECSCRM 2012*. to be published. 2012.

[GS22] W. Gerlach and O. Stern. "Der experimentelle Nachweis der Richtungsquantelung im Magnetfeld." In: *Zeitschrift für Physik A Hadrons and Nuclei* 9.1 (1922), pp. 349–352.

[Hal52] R.N. Hall. "Electron-Hole Recombination in Germanium." In: *Physical Review* 87 (1952), p. 387.

[HH89] P. Horowitz and W. Hill. *The art of Electronics - 2nd Edition*. Cambridge University Press, 1989.

[Koc09] M. Koch. "Coherent Spin Manipulation and ESR on Superfluid Helium Nanodroplets." In: *Physical Review Letters* 103 (2009).

[KR09] M. Koch and M. Ratschek. *Mikrowellentechnik für Spinresonanzexperimente - Laboratory Manual*. 2009.

[Krz+97] J. Krzystek et al. "DPPH as a standard for High-Field EPR." In: *Journal of Magnetic Resonance* 125 (1997), pp. 207–211.

[KSM78] D. Kaplan, I. Solomon, and N.F. Mott. "Explanation of the Large Spin-Dependent Recombination Effect in Semiconductors." In: *Le Journal de Physique - Lettres* 39 (1978), pp. 51–54.

[Lan74] D.V. Lang. "Deeplevel Tansient Spectroscopy: A New Method to Characterize Traps in Semiconductors." In: *Journal of Applied Physics* 45 (1974).

[Lép72] D.J. Lépine. "Spin-Dependent Recombination on Silicon Surface." In: *Physical Rev. B* 6.2 (1972), pp. 436–441.

[Lo11] C.C. Lo. "Electrical Detection of MAgnetic Resonance in Silicon." PhD thesis. University of California, Berkeley, 2011.

[LP70] D.J. Lépine and J.J. Préjean. In: *Proceedings of the 9th International Conference on the Physics of Semiconductors, Boston*. 1970.

[LSS11] A. Lund, S. Shimada, and M. Shiotani. *Priciples and applications of ESR spectroscopy*. Springer, 2011.

[LTK77] V.S. L'vov, O.V. Tretyak, and I.A. Kolomiets. "Spin-Dependent Carrier Recombination on a Silicon Surface." In: *Soviet Physics - Semiconductors* 11 (1977), pp. 661–664.

[ML00] T.D. Mishima and P.M. Lenahan. "A spin-depndent recombination study of radiation-induced Pb1 centers at the (001) Si/SiO_2 interface." In: *IEEE transactions on nuclear science* 47 (2000), pp. 2249–2255.

[Mue] John S Muenter. *Chemistry 232 - Molecular Spectroscopy, Laboratory Manual*.

[Odo+06] B. Odom et al. "New Measurement of the Electron Magnetic Moment Using a One-Electron Quantum Cyclotron." In: *Physical Review Letters* 97 (2006).

[Poo96] J.P. Poole. *Electron Spin Resonance - A Comprehensive Treatise on Experimental Techniques*. Dover Publications, 1996.

[PTP46] E.M. Purcell, H.C. Torrey, and R.V. Pound. "Resonance absorbtion by nuclear magnetic moments in a solid." In: *Pysical Review* 69 (1946), pp. 37–38.

[Rab+38] I.I. Rabi et al. "A new method of measuring nuclear magnetic moment." In: *Physical Review* 53.4 (1938), p. 318.

[Sah62] C.T. Sah. "Effect of Surface Recombination and Channel on P-N Junction and Transistor Characteristics." In: *IRE Transaction on Electron Devices* 9 (1962), pp. 94–108.

[SBK77] I. Solomon, D. Biegelsen, and J.C. Knights. "Spin Dependent Photoconductivity in the *n*-Type and *p*-Type Amorphous Silicon." In: *Solid State Communications* 22 (1977), pp. 505–508.

[Sch06] D.K. Schroder. *Semiconductor Material and Device Characterization*. 3rd ed. John Wiley & Sons, 2006.

[SGS95] B. Stich, S. Greulich-Weber, and J.-M. Spaeth. "Electrical Detection of Electron Paramagnetic Resonance: New Possibilities for the Study of Point Defects." In: *Journal of Applied Physics* 77 (1995).

[Shu90] M. Shur. *Physics of Semiconductor Devices*. Prentice Hall, 1990.

[SN07] S.M. Sze and Kwok K. Ng. *Physics of Semiconductor Devices*. 3rd ed. John Wiley & Sons, 2007.

[Sol76] I. Solomon. "Spin Dependent Recombination in a Silicon p-n Junction." In: *Solid State Communications* 20 (1976), pp. 215–217.

[Spa98] J.-M. Spaeth. *Identification of Defects in Semiconductors*. Ed. by M. Stavola. Vol. 51A. Semiconductors and Semimetals. Academic Press, 1998.

[SR52] W. Shockley and W.T. Read. "Statistics of the Recombination of Holes and Electrons." In: *Physical Review* 87.5 (1952), pp. 835–842.

[WB07] J.A. Weill and J.R. Bolton. *Electron paramagnetic resonance - elementary theory and applications*. 2nd ed. John Wiley & Sons, 2007.

[Zav45a] E. Zavoisky. "Paramagnetic relaxation of liquid solutions for perpendicular fields." In: *Journal of Physics* 9 (1945), pp. 211–216.

[Zav45b] E. Zavoisky. "Spin-magnetic resonance in paramagnetic substances." In: *Journal of Physics* 9 (1945), p. 245.

[Zee97] P. Zeeman. "On the influence of magnetism on the nature of the light emitted by a substance." In: *Philosophical Magazine* 43 (1897), p. 226.

Acronyms

D^0A^0 pair uncharged, exchange coupled donor-acceptor pair.

***G-R*-center** generation-recombination-center.

AC alternating current.

ADC analog-to-digital-converter.

AFC automatic frequency-controll.

Ag silver.

B boron.

BNC Bayonet Neill Concelman.

c-axis crystalline c-axis.

ClO_2 chlorine dioxide.

DAC digital-to-analog-converter.

DC direct current.

DLTS deep level transient spectroscopy.

DPPH 2,2-diphenyl-1-picrylhydrazyl.

EDMR electrically detected magnetic resonance.

ENDOR electron nuclear double-resonance.

EPR electron paramagnetic resonance.

ESD electrostatic discharge.

ESEEM electron spin echo modulation.

ESR electron spin resonance.

Fig. Figure.

Ge germanium.

H hydrogen.

He helium.

IV current-voltage.

KSM Kaplan-Solomon-Mott.

MOS metal oxide semiconductor.

MOSFET MOS field effect transistor.

N nitrogen.

NMR nuclear magnetic resonance.

NO nitric oxide.

NO_2 nitrous oxide.

O_2 diatomic oxygen.

ODMR optically detected magnetic resonance.

P phosphorus.

PCB printed circuit board.

RF radio frequency.

SDR spin dependent recombination.

Si silicon.

SiC silicon carbide.

SiO_2 silicon dioxide.

SNR signal-to-noise ratio.

TE transverse electric mode.

TEM transverse electromagnetic mode.

TM transverse magnetic mode.

Symbols

Symbol	Description	Unit
A	Area of the modulation loop	cm^2
B	Magnetic field (magnetic flux density)	G
B_{hfs}	Anistotropic hyperfine constant	G
B_{mod}	Modulation field amplitude	G
B_{static}	Static B field	G
C	Total creation rate of spin-pairs	$\mathrm{cm}^{-3}\,\mathrm{s}^{-1}$
E	Electric field	V/cm
E_{C}	Energy of the conduction band	eV
E_{V}	Energy of the valence band	eV
E_{i}	Intrinsic Fermi energy	eV
E_{m}	Energy of a magnetic moment in a magnetic field	eV
E_{np}	Electric field at the location of maximum recombination	V/cm
E_{t}	Energy of the trap	eV
E_{Fn}	Fermi energy of the electrons	eV
E_{Fp}	Fermi energy of the holes	eV
G	Generation probability of spin-pairs	s^{-1}
H	Magnetic field	A/cm
I	Nuclear spin quantum number	
I_{ind}	Induced current	A
J	Current density	$\mathrm{A/cm}^2$
J_0	Saturation current density	$\mathrm{A/cm}^2$
J_{i}	Current density throught an ideal p-n junction	$\mathrm{A/cm}^2$
J_{re}	Recombination current density	$\mathrm{A/cm}^2$
L	Angular momentum of a particle	N m
L_{z}	Angular momentum in z direction	N m
$N(\theta)$	Steady state density of pairs with angle θ	cm^{-3}
N_0	Occupancy of spin-pair with total spin 0	cm^{-3}
N_1	Occupancy of spin-pair with total spin 1	cm^{-3}
N_+	Occupancy of the energetically higher state	cm^{-3}
N_-	Occupancy of the energetically lower state	cm^{-3}
N_{A}	Acceptor density	cm^{-3}
N_{C}	Effective density of states in the conduction band	cm^{-3}
N_{D}	Donor density	cm^{-3}
N_{V}	Effective density of states in the valence band	cm^{-3}
N_{t}	Density of traps	cm^{-3}
N_{-1}	Occupancy of spin-pair with total spin -1	cm^{-3}
$N_{\mathrm{Sat}}(\theta)$	Steady state density of spin-pairs	cm^{-3}

Symbol	Description	Unit
P_{MW}	Microwave power	mW
P_{cavity}	Power in a cavity	mW
P_{input}	Input power	mW
Q	Quality factor of a cavity	
Q_0	Measured unloaded Q	
$Q_\perp$	Measured Q with c-axis perpendicular to z	
Q_{u}	Unloaded Q	
$Q_{\|\|}$	Measured Q with c-axis parallel to z	
R	Recombination rate	$\mathrm{cm}^{-3}\,\mathrm{s}^{-1}$
R_{loop}	Resistance of the modulation loop	Ω
R_{Sat}	Saturated recombination rate	$\mathrm{cm}^{-3}\,\mathrm{s}^{-1}$
S	Total spin	
$SNR_\perp$	SNR with c-axis perpendicular to z	
$SNR_{\|\|}$	SNR with c-axis parallel to z	
S_{EDMR}	EDMR signal	
T	Temperature	K
U_{ind}	Induced voltage	V
V	Voltage	V
V_{bi}	Built-in voltage	V
V_{sweep}	Controll voltage for sweeping the scan coils	V
W_{D}	Dissociation probability of a spin-pair	s^{-1}
W_{R}	Recombination probability	s^{-1}
$W_{\mathrm{R}}(\theta)$	Angular dependent recombination probability of a spin-pair	s^{-1}
W_{S}	Recombination probability of a pure singlet pair	s^{-1}
W_{ESR}	Transition probability between the N_{-1}, N_1 and N_0 states	s^{-1}
X	Component of phase detector output	V
X_{N}	Position of the nucleus	cm
Y	Component of phase detector output	V
ΔB	B field instability	G
ΔB_{scan}	Scan range	G
ΔE	Energy difference between two states	eV
ΔJ	Change of the current density	$\mathrm{A/cm}^2$
ΔR	Change of the recombination rate	$\mathrm{m}^{-3}\,\mathrm{s}^{-1}$
ΔW_{R}	Change of the recombination probability	s^{-1}
Φ	Flux though modulation loop	V s
Σ	Capture cross section of an electron being trapped by a G-R-center.	cm^2
δ	Skin depth	cm
ϵ	Electric constant, $\epsilon = 8.854 \cdot 10^{-12}\,\frac{\mathrm{A\,s}}{\mathrm{V\,m}}$	
η	Ideality factor	
γ	Gyromagnetic ratio	A s/kg
λ	Ratio of dissociation probability W_{D} and singlet creation probability W_{S}	
μ	Magnetic moment of a particle	$\mathrm{A\,m}^2$
μ_0	Magnetic constant, $\mu_0 = 1.257\,\frac{\mathrm{A\,s}}{\mathrm{V\,m}}$	
μ_{B}	Bohr magneton, $\mu_{\mathrm{B}} = 5.788 \cdot 10^{-5}\,\mathrm{eV/T}$	
μ_{N}	Nuclear magneton, $\mu_{\mathrm{N}} = 3.152 \cdot 10^{-8}\,\mathrm{eV/T}$	
μ_{r}	Relative permittivity	

Symbol	Description	Unit
ν	Microwave frequency	Hz
ν_0	Resonant frequency	Hz
ν_L	LARMOR frequency	Hz
ν_TE	Minimum propagable frequency of a TE mode	Hz
ν_ij	Minimum propagable frequency of an ij mode	Hz
ν_FWHM	Full width at half maximum of the cavity resonance peak	Hz
ω	Angular frequency	Hz
ω_L	LARMOR angular frequency	Hz
ϕ	Phase of phase detector output	
$\rho\,(X_\mathrm{N})$	Unpaired electron density	cm^{-3}
σ	Conductivity	$\Omega^{-1}\,\mathrm{cm}^{-1}$
σ_0	Capture cross section of charge carriers	cm^2
σ_B	Standard deviation of B field instabilities	G
σ_n	Capture cross section of electrons	cm^2
σ_p	Capture cross section of holes	cm^2
τ	Charge carrier lifetime	s
τ_1	Spin relaxation time	s
τ_2	Phase relaxation time	s
τ_LP	Time constant of a lock-in-amplifier	s
τ_cn	Capture time constant for electrons	s
τ_cp	Capture time constant for holes	s
τ_en	Emission time constant for electrons	s
τ_ep	Emission time constant for holes	s
$\mathbf{A}$	Area vector	cm^2
$\mathbf{B}$	Magnetic field vector	G
$\mathbf{B}_1$	Magnetic component vector of a photon	G
$\mathbf{B}_\mathrm{local}$	Local field vector produced by nearby magnetic moments	G
$\mathbf{B}_\mathrm{eff}$	Effective magnetic field for a bound electron	G
$\mathbf{D}$	Displacement vector	$\mathrm{A\,s/cm}^2$
$\mathbf{E}$	Electric field vector	V/cm
$\mathbf{E}_\mathrm{z}$	Electric field component in z_MW direction	V/cm
$\mathbf{H}$	Magnetic field vector	A/cm
$\mathbf{H}_\mathrm{z}$	Magnetic field component in z_MW direction	A/cm
$\mathbf{J}$	Current density vector	$\mathrm{A\,s/cm}^2$
$\mathbf{L}$	Angular momentum vector of a particle	N m
$\boldsymbol{\mu}$	Magnetic moment vector of a particle	$\mathrm{A\,m}^2$
θ	Angle between a pair of spins	
a	Expansion in x_MW direction	cm
a_hfs	Isotropic hyperfine constant	G
b	Expansion in y_MW direction	cm
c	Speed of light, $c = 3 \cdot 10^8 \mathrm{m/s}$	
d	Expansion in z_MW direction	cm
f_mod	Modulation frequency	Hz
g	LANDÉ g-factor	
g_0	Generation rate of charge carriers	$\mathrm{cm}^{-3}\,\mathrm{s}^{-1}$
$g_\perp$	g with c-axis perpendicular to B	
g_N	Nuclear g-factor	
g_e	LANDÉ g-factor of the free electron, $g_\mathrm{e} = 2.002319$	
g_x	g-factor in the x direction	

Symbol	Description	Unit
g_y	g-factor in the y direction	
g_z	g-factor in the z direction	
$g_{\|\|}$	g with c-axis parallel to B	
h	PLANCK constant, $h = 4.136 \cdot 10^{-15}\,\mathrm{eV\,s}$	
i	Mode number in x_MW direction	
j	Mode number in y_MW direction	
k_B	Boltzmann constant $k_\mathrm{B} = 8.617 \cdot 10^{-5}\mathrm{eV/K}$	
k_x	Wavenumber in x_MW direction	cm^{-1}
k_y	Wavenumber in y_MW direction	cm^{-1}
k_z	Wavenumber in z_MW direction	cm^{-1}
l	Angular momentum quantum number	
m	Mode number in z_MW direction	
m_I	z component of nuclear-spin angular-momentum vector	
m_e	Mass of an electron, $m_\mathrm{e} = 9.109 \cdot 10^{-31}\,\mathrm{kg}$	
m_l	Magnetic quantum number	
m_s	Spin projection quantum number	
n	Electron concentration	cm^{-3}
n_i	Intrinsic charge carrier concentration	cm^{-3}
p	Hole concentration	cm^{-3}
p_e	Magnetic polarization of an electron	
p_h	Magnetic polarization of a trapped hole	
q_e	Elementary charge, $q_\mathrm{e} = 1.602 \cdot 10^{-19}\mathrm{A\,s}$	
r	Amplitude of phase detector output	V
s	Spin quantum number	
t	Time	s
t_scan	Scan time	s
v_th	Thermal velocity of the charge carriers	cm/s
w_d	Depletion width	cm
x	x direction (perpendicular to the magnetic field)	cm
x_MW	Direction perpendicular to the z_MW	cm
y	y direction (perpendicular to the magnetic field)	cm
y_MW	Direction perpendicular to the z_MW	cm
z	z direction (direction of the applied magnetic field)	cm
z_MW	Direction of propagation of a microwave in a waveguide	cm

Equipment

Drusch RMN2 NMR magnetometer.

EA-PS 3032-10B Laboratory power supply.

HP 5255A Frequency converter.

HP 5335A Frequency counter.

HP 6269B Analog DC power supply.

Jäger ADwin Pro II Eight channel ADC-DAC.

Keithley 196 Digital multimeter.

Phillips FR 153 Audio amplifier.

Stanford Research SR 830 Digital lock-in-amplifier.

Stanford Research SR570 Current amplifier.

TTi QPX1200 Digital DC power supply.

Tektronix TDS 2004B Digital oscilloscope.

Varian E-101 X band microwave bridge.

Varian E-232 TE_{104} dual cavity.

Varian E9 ESR spectrometer.

Varian V-FR2503 Analog DC Power supply.

Varian V3400 9 inch electromagnet system.

List of Figures

List of Tables